An Assessment of Computational Procedures for Eleven-Stage Compressor Response to Inlet Distortion

by

Keen Ian Chan

B. Eng., Mechanical & Production Engineering (1997)

Nanyang Technological University,
Singapore

Submitted to the Department of Aeronautics and Astronautics
in partial fulfillment of the requirements for the degree of
Master of Science in Aeronautics and Astronautics

at the

Massachusetts Institute of Technology

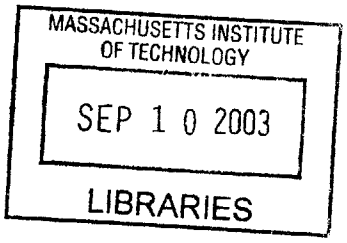

June 2003

Signature of Author .....
Department of Aeronautics and Astronautics
May 12, 2003

Certified by .....
Yifang Gong, PhD
Research Engineer
Thesis Supervisor

Certified by .....
Choon S. Tan, PhD
Senior Research Engineer
Thesis Supervisor

Accepted by .....
Edward M. Greitzer, PhD
H. N. Slater Professor
Chair, Department Committee on Graduate Students

An Assessment of Computational Procedures for Eleven-Stage Compressor Response to Inlet Distortion

by

Keen Ian Chan

Submitted to the Department of Aeronautics and Astronautics
on May 12, 2003, in partial fulfillment of the requirements for the degree of
Master of Science in Aeronautics and Astronautics.

ABSTRACT

Streamline curvature data for an 11-stage compressor was used to establish a row-by-row body force representation of the compressor. This representation was then incorporated into an existing computational methodology for compressor performance. The computed results from the computational methodology are in accord with the streamline curvature results, demonstrating the validity of the approach.

A body force formulation, previously demonstrated for its adequacy in reproducing the performance characteristics of cascades, has been used to represent an 11-stage compressor for incorporation into the above computational methodology. This was used to determine the 11-stage compressor response to an inlet distortion of 180^0 circumferential extent for contrasting against its performance under uniform inlet flow.

Using the computed results at the inlet to and outlet of the compressor, the computed total pressure ratio and efficiency for the clean condition are 14.22 and 76.9% respectively. Similarly, for the distorted case, these are 10.35 and 71.8% respectively, showing a deterioration in efficiency of 5%. The deterioration is found to be 4.5% when losses generated in the blade rows are considered. The discrepancy of 0.5% can be accounted for by the numerical dissipation in gaps between blade rows and the blade rows themselves. The deterioration is found to be 5.2% when the former is taken into account, the latter has not been considered.

Thesis Supervisors: Yifang Gong, Research Engineer
Department of Aeronautics and Astronautics

Choon S. Tan, Senior Research Engineer
Department of Aeronautics and Astronautics

ACKNOWLEDGMENTS

I would like to express my heartfelt thanks and appreciation to Dr. Choon S. Tan for his invaluable advice and guidance. Special thanks is also expressed to Dr. Y. Gong, whose previous work is the foundation for this project, and for providing insightful comments and computational tools. I also wish to thank Dr. T. Shang of Pratt & Whitney Aircraft Engines for his support and technical comments.

I am especially grateful to my wife Serene for her love and faithful support. Her encouragement and prayers have provided me with much inspiration. I am also grateful to my parents, for their encouragement and valuable advice. Special thanks is also expressed to my brother, Keen Len, and sister, Gwen, for their caring and encouraging support.

Fellow students at MIT have made my time here a memorable one. I have enjoyed the friendship of fellow students at GTL, in particular, Neil Murray, Joe Lee, Parthiv Shah, Alexis Manneville, Chiang Juay Teo and Andrew Luers.

This project was supported by Singapore Technologies Aerospace, Pratt & Whitney Aircraft Engines and NASA-Glenn (grant number NAG3-2101).

CONTENTS

1. **INTRODUCTION** 14
   - 1.1 Technical Background 14
   - 1.2 Technical Objectives 18
   - 1.3 Contributions of the Thesis 19
   - 1.4 Thesis Organization 20

2. **TECHNICAL APPROACH AND METHODOLOGY** 21
   - 2.1 Governing Equations 21
   - 2.2 Advantages and Limitations for the Use of Body Forces 22
   - 2.3 Procedure for Computing the Body Forces 23
   - 2.4 Description of the 11-stage W40 Axial Compressor 24
   - 2.5 Implementation of Methodology for Axisymmetric Computations 25
   - 2.6 Implementation of Methodology for Computing Compressor Response to Inlet Distortion 28
   - 2.7 Chapter Summary 30

3. **RESULTS AND DISCUSSION FOR AXISYMMETRIC COMPUTATIONS** 31
   - 3.1 CFD Results and Comparison with Streamline Curvature Data 31
     - 3.1.1 Overall Performance 31
     - 3.1.2 Stage Performance 32
     - 3.1.3 Radial Flow Profiles 33
   - 3.2 Chapter Summary 35

4. **RESULTS AND DISCUSSION FOR INLET DISTORTION COMPUTATIONS** 36
   - 4.1 Results for Compressor Performance 37
     - 4.1.1 Overall Performance 37
     - 4.1.2 Stage Performance 42
   - 4.2 Static Pressure at Compressor Outlet 44
   - 4.3 Distortion Behavior from Upstream Boundary to IGV Inlet 45
     - 4.3.1 Formation of Static Pressure Distortion at IGV Inlet 46
     - 4.3.2 Asymmetric Character of the Velocity Distortion at the IGV Inlet 49
   - 4.4 Distortion Propagation Through Compressor Stages 50
     - 4.4.1 Amplification of Static Pressure Distortion Through First 9 Stages 51
     - 4.4.2 Attenuation of Static Pressure Distortion Through Last 2 Stages 52
   - 4.5 Chapter Summary 56

5. **SUMMARY, CONCLUSIONS AND FUTURE WORK** 58
   - 5.1 Summary 58
   - 5.2 Conclusions 59
   - 5.3 Recommendations for Future Work 60

A. DERIVATION OF GOVERNING EQUATIONS 62

B. CALCULATION OF BODY FORCES FROM STREAMLINE CURVATURE DATA 72

BIBLIOGRAPHY 74

LIST OF FIGURES

Fig. 2.1	Configuration of 11-stage Axial Compressor	25
Fig. 2.2	Control Volume with Body Force	26
Fig. 2.3	Mesh for the 11-stage Compressor (342x80x12)	27
Fig. 3.1	Graph of Compressor Stage Performance	33
Fig. 3.2	Radial Profiles for R15 Showing that the Computed Data Does Not Exactly Agree with Streamline Curvature Data	34
Fig. 4.1	Distribution of Entropy Rise Across the Stages for (a) Clean Inlet Flow (b) Distorted Inlet Flow	41
Fig. 4.2	Deterioration in Stage Total Pressure Ratio	42
Fig. 4.3	Deterioration in Efficiency	43
Fig. 4.4	Computed Mid-radius Static Pressure at Compressor Exit	45
Fig. 4.5	Variation of Pressure Rise with Flow Coefficient	46
Fig. 4.6	Static Pressure Distortion at the Mid-radius of the IGV Inlet	47
Fig. 4.7	Mid-radius Velocity Distributions at (a) Upstream Boundary and (b) IGV Inlet, Showing Attenuation of the Velocity Distortion at the IGV Inlet	48
Fig. 4.8	Total Pressure at Mid-Radius of the IGV Inlet, Showing Reduction of Circumferential Extent of Low Total Pressure Region from Upstream Boundary to IGV Inlet	48
Fig. 4.9	Flow Angles at IGV Inlet, Showing Induced Swirl	49
Fig. 4.10	Range of Static Pressure for Each Stage, with the Circled Region	51

Showing Strong Attenuation in Static Pressure Distortion Across the Last 2 Stages

Fig. 4.11 Amplification of Static Pressure Distortion, as Shown by Mid-radius Static Pressure at (a)Stage 1 Inlet, (b)Stage 3 Inlet, (c) Stage 5 Outlet and (d)Stage 9 Outlet 52

Fig. 4.12 Elimination of Static Pressure Distortion Across Stage 11, Showing Regions in which Pressure is Reduced 54

Fig. 4.13 Total Pressure at R15 Inlet and EGV Exit (Stage 11 Inlet and Outlet Respectively), Showing Regions in which Total Pressure is Reduced 55

Fig. 4.14 Total Pressure Rise Across Each Stage, Showing that Total Pressure Actually Falls Across Stage 11 (Circled). Total Pressure Rise for a Stage is Defined as $\frac{P_{t,outlet} - P_{t,inlet}}{\frac{1}{2}\rho U^2}$ 56

Fig. A.1 Integration Path for Pitchwise Averaging 63

Fig. A.2 Definition of $\Delta\theta_0$ 65

Fig. A.3 Pressure and Viscous Loading at a Typical Point 69

Fig. B.1 Control Volume with Body Force 72

LIST OF TABLES

Table 3.1	Compressor Overall Performance	31
Table 3.2	Compressor Stage Performance	32
Table 4.1	Compressor Performance for Axisymmetric and Distorted Inlet Flow	37
Table 4.2	Adiabatic Efficiency Calculated from Losses in Blade Rows and Gaps	39

In loving memory of

my Dad, Mr Eden Chan

and

Aunt Joanne

CHAPTER 1 : INTRODUCTION

1.1 Technical Background

The availability of computer resources and advancements in CFD algorithms has enabled the computations of three-dimensional flow in turbomachinery flow paths. Applications include the design and analysis of turbomachinery components (compressors and turbines) [3,4]. More recently there has been increasing use of CFD as a research tool (e.g. Ref. [9]). However, because of the challenges posed by the flow environments associated with multistage turbomachines, various degrees of physical approximations have been developed to enable the computation of such flows. These range from use of the streamline curvature method [7,17] and matrix throughflow analysis [24] to three-dimensional Reynolds-averaged Navier-Stokes analysis that uses mixing plane approximation between blade rows to enable multistage computations [6,8,10]. More recently there have been attempts to compute 3-dimensional unsteady viscous flow in the multi-blade rows environment but these are mostly confined to feasibility demonstrations or the generation of flow fields to answer specific research questions [26]. The level of physical approximation one should adopt depends on the technical problem being addressed [13].

There has been a drive toward developing a framework for compressor design and analysis that takes advantage of modern CFD and the ability to model blade-passage flow processes that would have been computationally demanding if computed within the multi-blade-row environment. Ideally such a framework should have the capability of

generating the performance map including the operability limit. Such a capability would represent an improvement over the streamline curvature method, whose physical and engineering adequacy is dependent on empirical models for loss generation [1,17].

The framework for this work is based on the fact that the action of a blade row brings about pressure rise, flow turning and energy exchanges, and that these effects can also be brought about by replacing the blade row with a body force field. The resulting governing equations are a set of flow equations (Euler or Navier-Stokes) with the addition of body force terms that appear as source terms to the flow equations. The requirements for the body force representation of a blade row are:

1. It must satisfy conservation of mass, momentum and energy
2. There must be correct dependence on geometry
3. It must reproduce the overall pressure rise and turning angle
4. It must respond locally to unsteady three-dimensional flow variations

The concept of using body force distribution to represent a blade row is not new. It has been previously used by Marble [23], Smith [25], Horlock and Marsh [18] and Adamczyk [2]. The present work is an extension of the recent uses of the body force representation by Gong [13] and Choi [5]. Marble [23] developed an axisymmetric body force model for throughflow computations in blade rows. This body force can be viewed as the distribution of the force applied by the blade on the flow, and can be decomposed into a normal pressure force and a tangential shear force. Smith [25] derived an equation that described the radial variation of circumferential-average flow properties inside a

blade row. The equation contains terms associated with physical effects such as centripetal acceleration, meridional streamline curvature, blockage gradient and isentropic density change. Horlock and Marsh [18] showed, by averaging the two-dimensional differential form of the continuity and momentum equations across a blade passage, that two-dimensional blade rows in steady inviscid flow can be replaced by distributed body forces. Adamczyk [2] showed by applying three averaging operators on the three-dimensional unsteady Navier-Stokes equations that unsteadiness resulting from a multi-blade row environment can be captured by a steady computation using distributed body forces, heat sources and deterministic stresses. The model elements are obtained by the application of a closure model, in the same way as a turbulence model is used to obtain Reynolds stresses in a turbulent flow computation.

Gong [13] developed a computational model using body forces for determining the response of multistage compressors to inlet distortion, and for simulating the inception and development of rotating stall in axial compressors. The model involves representing each blade row with a continuously distributed body force field which produces the effects of pressure rise and flow turning of the blade row. The body forces are determined from experimental data. The representation is similar to using an infinite number of blades, with locally axisymmetric flow in each infinitesimal blade passage. The flow fields between any two blade passages can be different, thus allowing a circumferentially non-uniform flow field to be represented by an infinite number of axisymmetric flow fields. Such a compressor model is suitable for assessing the response of compressors to circumferential flow non-uniformity with length scales larger than a blade pitch. The

model has been demonstrated in the capturing of experimentally observed flow phenomena, such as the development of rotating stall via short wavelength disturbances and the switch from long to short wavelength stall inception resulting from the restaggering of inlet guide vanes.

In an application for compressor map generation, Choi [5] formulated and implemented a computational methodology that extracts body forces from CFD data, rather than from experimental data. The method proposes that each blade row of a multistage compressor be taken in isolation for Navier-Stokes computations over a range of operating points. A body force database is thus generated for each blade row. Upon assembling the individual databases together, the body force representation for the multistage compressor is obtained. The response of a compressor to off-design or distorted inlet flow is then computed with the body force databases embedded as source terms in the Euler equations. The methodology has been implemented to compute the performance characteristics and the response under radial flow distortion of an isolated transonic rotor.

While Choi [5] demonstrated the extraction of the body force representation on a rigorous basis from Navier-Stokes data, for the situation of multi-stage compressor with a large number of blade rows (e.g. the 11-stage compressor investigated in this work has 23 blade rows), the method requires a large number of Navier-Stokes computations to generate the body force representation. Streamline curvature methods, on the other hand, are more effective and when incorporated with adequate correlations, provide an analysis tool for multistage compressors. In this work, the extraction of the body force

representation from streamline curvature data is proposed. The method is implemented on an 11-stage compressor, and its consistency is demonstrated by reproducing an operating point in steady-state axisymmetric flow. In principle, the body force representation can be applied, in conjunction with a model which enables body forces to respond to local flow conditions, for inlet distortion computations. This was the original intended goal but it has not been implemented in this thesis. Instead, in the computations of compressor response to inlet distortion, the body force formulation of Gong [13] for determining body forces from local flow properties is used. The formulation is simple and has previously demonstrated its adequacy in reproducing the performance characteristics of cascades [21] and single-stage compressors [13]. As such, it is to be noted that one cannot make a statement on the utility of streamline curvature solution for establishing the body force representation of blade rows for use in assessing compressor response to inlet distortion.

1.2 Technical Objectives

The specific technical objectives are to:

1. Assess the utility of the blade-row-by-blade-row body force representation based on streamline curvature data of a multistage compressor with the intent of using it to assess the compressor response to inlet distortion.

2. Determine the evolution of a 180^0 circumferential inlet distortion in an 11-stage compressor and the associated flow field development based on a body force formulation developed by Gong [13][1].

1.3 Contributions of the Thesis

The following are the main contribution of the thesis:

- The use of streamline curvature data to derive the blade-row-by-blade-row body force representation of a multistage compressor. This is more efficient as compared to the use of Navier-Stokes results and can, in principle, be used to determine the compressor response to inlet distortion. However, the latter has not been implemented in this thesis.
- The use of the body force formulation of Gong [13] to compute, for an 11-stage compressor, (1) performance and flow field under clean inlet conditions and (2) the response to inlet distortion at the same corrected mass flow. For (1), the computed total pressure ratio and efficiency (using total pressure and total temperature ratios) are 14.22 and 76.9% respectively. For (2), these are 10.35 and 71.8% respectively, representing a decrement in efficiency of 5 % over that of (1). By calculating efficiency using the losses generated in blade rows by the body forces, the decrement is found to be 4.5%. The discrepancy of 0.5% can be accounted for by numerical

[1] The original intent was to use the body force representation of objective (1) together with a model for computing their response to unsteady variations in the flow field to compute compressor response to inlet distortion. This has not been done. The formulation mentioned here is not associated with the body force representation extracted from the streamline curvature solution. It is one that has previously demonstrated its adequacy in reproducing performance characteristics of cascades and single-stage compressors. Further details in Section 2.6.

dissipation in the gaps between blade rows and the blade rows themselves. The latter has not been taken into account.

1.4 Thesis Organization

Following this introduction, Chapter 2 presents the technical approach adopted in this work. This includes a discussion of key aspects of the body force representation. This is followed by a description of the implementation for axisymmetric and inlet distortion computations on an 11-stage compressor. Chapter 3 presents the results from axisymmetric computations and assesses the applicability of the blade-row-by-blade-row body force representation extracted from streamline curvature data. Chapter 4 presents the results from inlet distortion computations using the body force formulation of Gong [13] and analyzes the flow field for consistency. Chapter 5 presents a summary and states the conclusions.

CHAPTER 2 : TECHNICAL APPROACH AND METHODOLOGY

This chapter presents the framework for the use of body forces to represent blade row effects. This is followed by a presentation of the implementation of the methodology for computing the axisymmetric flow field and the response of an 11-stage compressor to inlet distortion.

2.1 Governing Equations

Within a blade row, by integrating the unsteady, three-dimensional, compressible Navier-Stokes equations in the circumferential direction, a system of unsteady two-dimensional equations in the *x-r* plane is obtained. The detailed derivation of the equations is presented in Appendix A. These equations contain terms which can be shown, as described in Appendix A, to be "body forces". The resulting equations incorporating body forces are given by

$$\frac{\partial(b\overline{U})}{\partial t}+\frac{\partial(b\overline{F}_{inv})}{\partial x}+\frac{\partial(b\overline{H}_{inv})}{\partial r}=b\overline{S}+\overline{F} \tag{2.1}$$

where the overbar represents a circumferentially averaged property, and

$$\overline{U}=\begin{vmatrix} r\overline{\rho} \\ r\overline{\rho}\overline{V}_x \\ r\overline{\rho}\overline{V}_\theta \\ r\overline{\rho}\overline{V}_r \\ r\overline{\rho}\overline{e}_t \end{vmatrix},\ \overline{F}_{inv}=\begin{vmatrix} r\overline{\rho}\overline{V}_x \\ r\left(\overline{\rho}\overline{V}_x^{\,2}+\overline{p}\right) \\ r\overline{\rho}\overline{V}_x\overline{V}_\theta \\ r\overline{\rho}\overline{V}_x\overline{V}_r \\ r\overline{V}_x\left(\overline{\rho}\overline{e}_t+\overline{p}\right) \end{vmatrix},\ \overline{H}_{inv}=\begin{vmatrix} r\overline{\rho}\overline{V}_r \\ r\overline{\rho}\overline{V}_x\overline{V}_r \\ r\overline{\rho}\overline{V}_\theta\overline{V}_r \\ r\left(\overline{\rho}\overline{V}_r^{\,2}+\overline{p}\right) \\ r\overline{V}_r\left(\overline{\rho}\overline{e}_t+\overline{p}\right) \end{vmatrix},\ \overline{S}=\begin{vmatrix} 0 \\ 0 \\ -\overline{\rho}\overline{V}_\theta\overline{V}_r \\ \overline{\rho}\overline{V}_\theta^{\,2}+\overline{p} \\ 0 \end{vmatrix},\ \overline{F}=\begin{vmatrix} 0 \\ r\overline{\rho}f_x \\ r\overline{\rho}f_\theta \\ r\overline{\rho}f_r \\ r\overline{\rho}\left(\vec{f}\cdot\vec{V}\right) \end{vmatrix}$$

$\vec{f}$ is the body force per unit mass with components f_x, f_θ and f_r; and b is a blockage factor defined as the ratio of the angular pitch at a general point (x,r) to that at the leading edge.

Its value corresponds to 1 for blades with zero thickness and to some value less than 1 when blades of finite thickness are present.

Eq. (2.1) shows that the action of a blade-row on the flow may be represented by an axisymmetric flow field in pitchwise-averaged flow properties and an appropriately derived distributed body force $\vec{f}(x,r)$. Physically, this is equivalent to using an infinite number of blades, with the flow being axisymmetric in each infinitesimal blade passage. As described in Section 1.1, such a representation is adequate for assessing the response of a blade row or compressor to circumferential flow non-uniformity with length scale larger than a blade pitch.

In this work, Eq. (2.1) is solved numerically using the CFD code UnsComp [13] which couples the compressor with a plenum and throttle, consistent with the compression system model of Greitzer [14,15]. The equations are discretized spatially and, using zero flow and zero compressor speed conditions as the initial condition, are marched in time using the five-step Runge-Kutta time-marching scheme of Jameson et al [20]. The imposed boundary conditions are total pressure, total temperature and flow angles at the upstream boundary, as well as throttle setting.

2.2 Advantages and Limitations for the Use of Body Forces

The main advantage of the body force representation is the description of flow variation with length scales larger than a blade pitch at far less computational expense than a full three-dimensional computation of flow in blade row with individual discrete blade

passages. This renders computationally feasible such tasks as simulating the evolution of a stall cell and compressor response to inlet distortion. The condition on length scale also presents a limitation in that it cannot be used to investigate the role of blade passage events on the onset of compressor instability.

As shown in the derivation in Appendix A, an assumption had to be made before Eq. (2.1) could be obtained from the pitchwise-averaged Navier-Stokes equations. The assumption is that the blades are thin, and that the slopes of the pressure and suction surfaces are approximately equal. This assumption does not hold at the leading and trailing edges.

2.3 Procedure for Computing the Body Forces

To illustrate the steps involved in the determination of body forces, an example is described in this section which involves computation of the forces from a three-dimensional steady-state flow field (for instance, this can be the result of a three-dimensional Navier-Stokes calculation)

- Construct the three-dimensional distribution of the flux variables F_{inv}, H_{inv} and the source term S
- Perform averaging in the pitch-wise direction to obtain the averaged flux quantities $\overline{F}_{inv}$, $\overline{H}_{inv}$ and $\overline{S}$
- Mesh the axisymmetric flow field with 2-dimensional finite volume cells

- Integrate Eq. (2.1) numerically without the time derivative term (this example involves steady-state conditions) over each finite volume cell. The body forces are thus obtained numerically at discrete points in the flow field

The first two points involve simplifying a three-dimensional flow field within a blade row into an axisymmetric flow.

2.4 Description of the 11-stage Axial Compressor

In this work, the body force representation is applied for axisymmetric and inlet distortion computations on an 11-stage axial compressor which is representative of current design. This comprises an IGV followed by 11 stages, leading to 23 blade rows in total. The configuration is shown in Fig. 2.1. The procedure for implementation of the body force representation is presented in Sections 2.5 and 2.6.

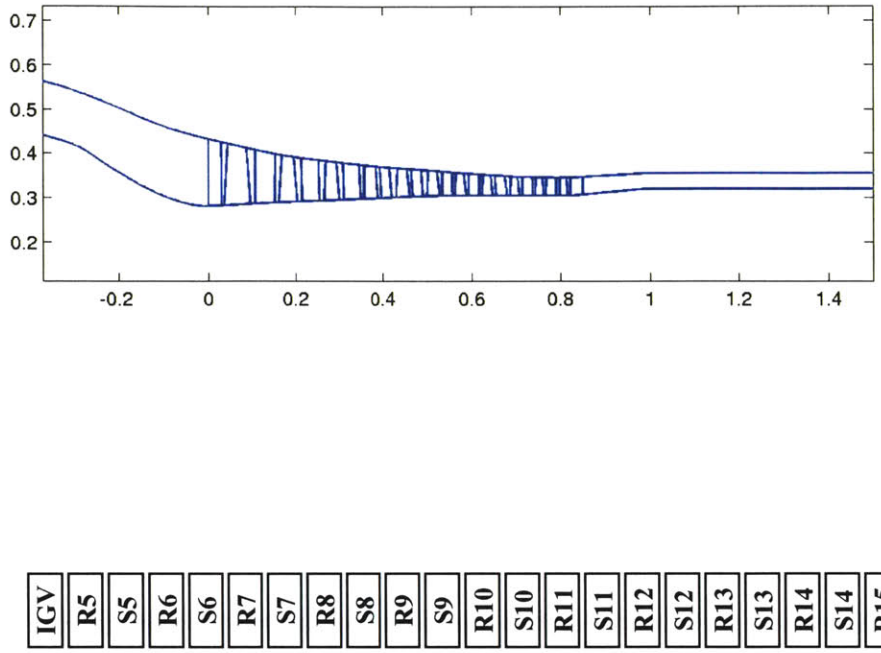

Fig. 2.1 Configuration of 11-stage Axial Compressor

2.5 Implementation of Methodology for Axisymmetric Computations

This section presents the procedure involved in implementing the blade-row-by-blade-row body force representation for computing the axisymmetric flow field and hence the performance of the 11-stage axial compressor (details given in previous section).

Streamline curvature [7] results were made available and these provided knowledge of the flow properties ($\bar{\rho}$, $\bar{p}$ etc.) and blockage at discrete points along the leading and trailing edges of each blade row. The operating point is defined by

Corrected mass flow = 57.08 kg/s

Corrected speed = 8082 rpm

Total Pressure Ratio = 10.94

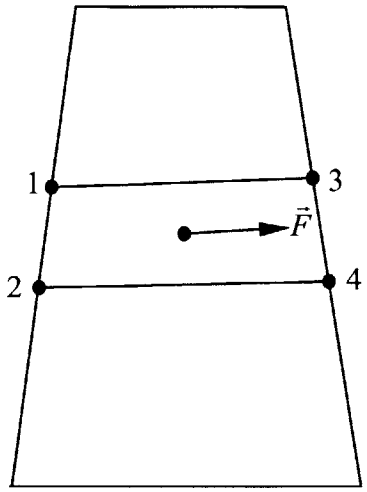

Fig. 2.2 Control Volume with Body Force

Fig. 2.2 shows a typical blade row with points 1, 2, 3 and 4 being points along the leading and trailing edges. The flow properties and blockage at these points are known from streamline curvature data. These points form a control volume which is acted upon by a total body force $\vec{F}$. By numerical integration of Eq. (2.1), $\vec{F}$ can be determined. The detailed procedure for this is presented in Appendix B.

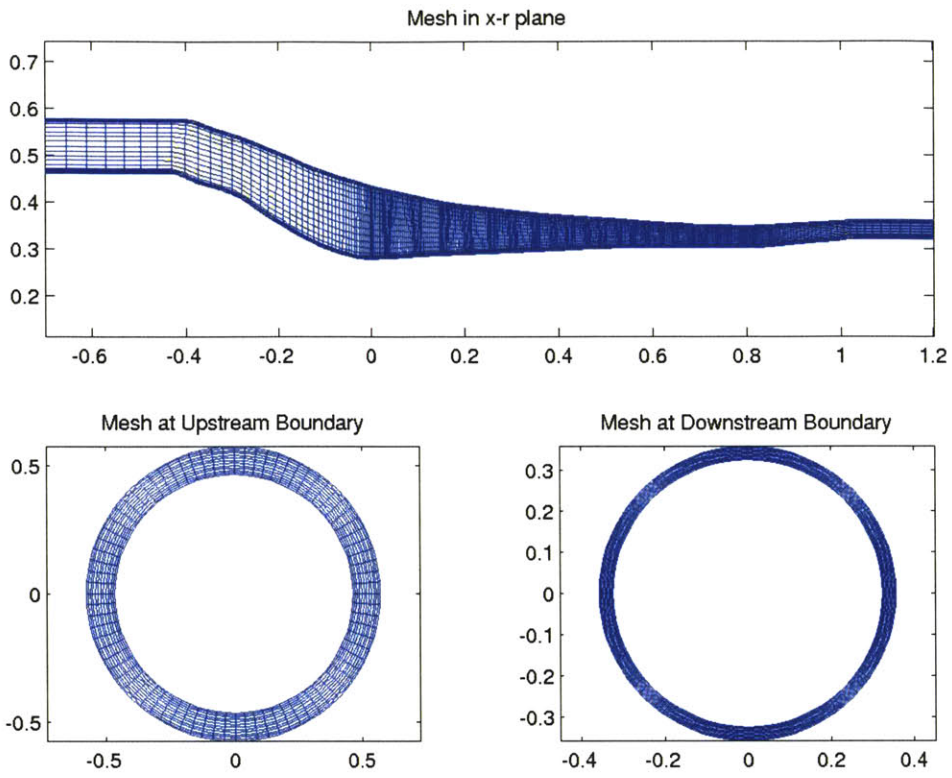

Fig. 2.3 Mesh for the 11-stage Compressor (342x80x12)

The flow domain is then meshed with a 342x80x12 grid as shown in Fig. 2.3. Only the mesh in the *x-r* plane (as shown in the top half of Fig. 2.3) is used in subsequent CFD calculations. Each control volume extending from the leading to trailing edge of a blade row, as typified by the quadrilateral 1234 in Fig. 2.2, now contains a number of computational cells along its axial length. The distribution of the force $\vec{F}$ among these cells is such that it meets the condition that the summation of the forces assigned to the cells equals the total force $\vec{F}$. The "hat" function is chosen here for simplicity and for the avoidance of computational difficulty. The cells are assigned forces which rise linearly from a small value at the leading edge to a peak value in the middle region, and then fall

linearly to a small value at the trailing edge. Such a distribution is chosen to avoid abrupt changes which can result in Gibbs phenomena, leading to numerical difficulty.

With the body forces known, Eq. (2.1) is solved numerically on this mesh using a CFD code (UnsComp, described in Section 2.1) to obtain the flow field at the same corrected mass flow and corrected speed as the streamline curvature data. Boundary conditions are imposed such that the computations converge at the same corrected mass flow and corrected speed as the streamline curvature data. These are total pressure, total temperature and flow angles at the upstream boundary, as well as throttle setting. The utility of using body forces to represent blade row effects would be assessed by comparison of the computed results with streamline curvature data. The results and discussion are presented in Chapter 3.

2.6 Implementation of Methodology for Computing Compressor Response to Inlet Distortion

For the case of inlet distortion, a total pressure distortion is imposed at the upstream boundary. The low and high total pressure regions each occupy a circumferential extent of 180^0 and the distortion is defined by $\frac{P_{t,high} - P_{t,low}}{\frac{1}{2}\rho U^2} = 0.49$. The flow field and total pressure ratio are computed at a corrected mass flow of 53.94 kg/s. To determine the effects of inlet distortion on the performance of the compressor, the total pressure ratio for an axisymmetric flow at the same corrected mass flow is computed. For both axisymmetric flow and inlet distortion, the transient phase of the computations require

the body forces to vary transiently in response to a time-varying flow field. The body force formulation of Gong [13] is used in this work to calculate body forces from knowledge of local flow conditions.

The local blade force comprises of 2 components, $\vec{F}_n$ which is normal to the blade and $\vec{F}_p$ which is parallel to the blade. $\vec{F}_n$ is considered to be due to the pressure loading and $\vec{F}_p$ the viscous shear. It can be shown that these force components depend on local flow properties. The relationship can be expressed as

$$\vec{F}_n = -K_n(\Delta\beta, M, \mathrm{Re})\frac{\left(\vec{V}_{rel}\cdot\hat{\eta}\right)\left(\vec{V}_{rel}\cdot\hat{\xi}\right)}{h}\hat{n} \tag{2.2}$$

$$\vec{F}_p = -K_p(\Delta\beta, M, \mathrm{Re})\frac{\vec{V}_{rel}\cdot\vec{V}_{rel}}{h}\hat{p} \tag{2.3}$$

K_n and K_p are coefficients which, in general, depend on local deviation angle $\Delta\beta$, Mach number M and Reynolds number Re. $\vec{V}_{rel}$ is the relative velocity vector. $\hat{\eta}$ and $\hat{\xi}$ are unit vectors parallel and normal to the blade surface respectively. $\hat{n}$ and $\hat{p}$ are unit vectors normal and parallel to $\vec{V}_{rel}$ respectively.

In this work, K_n and K_p are assumed constant and are determined from

$$K_n = 4.2 - 2\alpha \tag{2.4}$$

$$K_p = 0.04 \tag{2.5}$$

The use of Eqns. (2.4) and (2.5) is motivated by their simplicity and ability to reproduce loss and deviation trends in cascades [13,21]. A more rigorous approach would be to

calculate local values of K_n and K_p using the body force representation extracted from streamline curvature data and Eqns. (2.2) and (2.3). This was not carried out. The results and discussion of the compressor response to inlet distortion based on the formulation described by Eqns. (2.2) to (2.5) are presented in Chapter 4.

2.7 Chapter Summary

This chapter has presented the overall conceptual framework for the methodology for computing the performance of an 11-stage compressor in axisymmetric flow and its response to inlet distortion with a circumferential sector of 180^0 and the advantages and applicability of such an approach. The steps involved in implementing the methodology for computing the performance of the 11-stage compressor with axisymmetric upstream flow and inlet distortion are presented.

CHAPTER 3 : RESULTS AND DISCUSSION FOR AXISYMMETRIC COMPUTATIONS

This chapter presents computed results obtained from the implementation of the body force representation as described in Section 2.5. To assess the adequacy of the blade-row-by-blade-row body force representation as implemented here, comparisons between the computations and the reference streamline curvature data are made for overall performance, stage performance and radial flow profiles.

3.1 Computed Results and Comparison with Streamline Curvature Data

In subsequent sections, results from UnsComp are presented and compared with streamline curvature data. Overall performance is first discussed, followed by stage performance and finally, radial profiles of various flow properties at a selected axial location are examined.

3.1.1 Overall Performance

For overall performance, the operating point obtained by UnsComp is shown in Table 3.1 along with the reference streamline curvature data.

	Reference	**UnsComp**
Corrected Mass Flow (kg/s)	57.08	57.12
Corrected Speed (rpm)	8082	8082
Total Pressure Ratio	10.94	10.69

Table 3.1 Compressor Overall Performance

The total pressure ratio for the whole compressor as obtained by UnsComp represents an error of 2.3% as compared to the streamline curvature data. The overall performance is thus seen to be adequately reproduced by UnsComp.

3.1.2 Stage Performance

The total pressure ratio for each stage is presented in Table 3.2 which compares the total pressure ratio calculated by UnsComp with streamline curvature data. The stage pressure ratios are plotted in Fig. 3.1 and indicate that, although the body force representation is actually an approximation to the pitchwise-averaged Navier-Stokes equations (Section 2.2), the agreement is within 3% of the reference streamline curvature data.

Stage	Reference	UnsComp	% Error
1	1.54	1.50	-2.74
2	1.26	1.25	-1.12
3	1.28	1.27	-1.02
4	1.29	1.28	-0.82
5	1.22	1.21	-0.80
6	1.22	1.22	-0.01
7	1.21	1.22	0.72
8	1.20	1.22	1.33
9	1.19	1.20	0.79
10	1.17	1.17	0.27
11	1.14	1.15	0.95

Table 3.2 Compressor Stage Performance

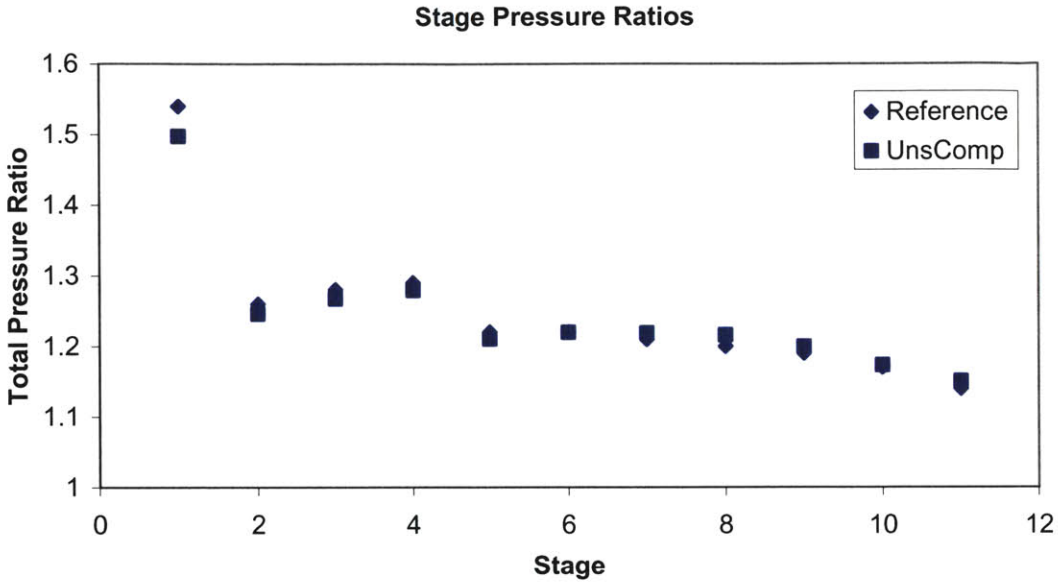

Fig. 3.1 Graph of Compressor Stage Performance

3.1.3 Radial Flow Profiles

In this section, radial flow profiles from UnsComp calculations are compared with corresponding streamline curvature data. The goal here is to assess the capability of the body force representation to compute detailed distributions of flow properties within the flow passage.

The radial profiles for the rotor R15 (shown in Fig. 3.2) serve as an example to illustrate that the two sets of data will not be in exact agreement. Increase in total pressure is defined as $\frac{P_{t,TE} - P_{t,LE}}{\frac{1}{2}\rho U^2}$ and increase in total temperature as $\frac{c_p\left(T_{t,TE} - T_{t,LE}\right)}{U^2}$ where the subscripts *TE* and *LE* denote trailing edge and leading edge values respectively.

r^* is a non-dimensional radial coordinate defined by

$$r^* = \frac{r - r_h}{r_t - r_h}$$

The subscripts h and t denote hub and tip respectively. The symbols 'o' and 'x' denote reference streamline curvature and UnsComp values respectively.

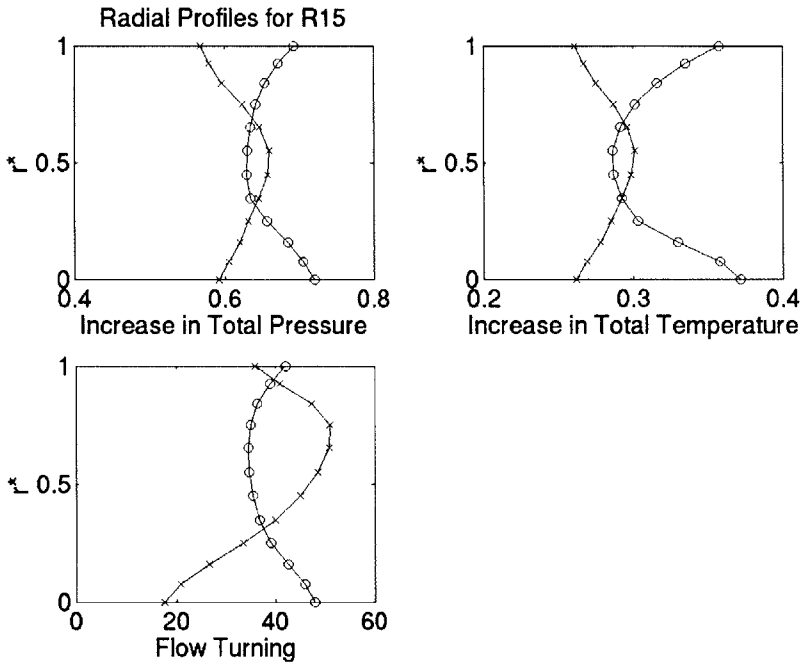

Fig. 3.2 Radial Profiles for R15 Showing that the Computed Data Does Not Exactly Agree with Streamline Curvature Data

It can be seen that while the radial profiles of the 2 sets of data do not match, the overall total pressure ratio of the whole compressor as presented in Section 3.1 is in agreement with the value from streamline curvature data (error of only 2.3%). This is due to the fact that the calculation for overall total pressure ratio is set by the integrated value of body force of the whole compressor.

3.2 Chapter Summary

The blade-row-by-blade-row body force representation of the 11-stage compressor has been extracted from streamline curvature data and incorporated in UnsComp computations. The end results are found to be in accord with the streamline curvature results. Therefore, the implementation in UnsComp is shown to be consistent with the streamline curvature data.

CHAPTER 4 : RESULTS AND DISCUSSION FOR INLET DISTORTION COMPUTATIONS

In this section, results for the calculation of the 11-stage compressor under circumferential inlet distortion are presented. The technical procedure has been presented previously in Section 2.8. The flow field is analyzed for self consistency as a means for assessing the applicability of the body force representation to determine the compressor response to inlet distortion. It is to be reminded that the body force representation of the blade rows in the 11-stage compressor is based on the formulation of Gong [13] (also see Eqns. (2.2) to (2.5)) and not that which was extracted from the streamline curvature data. The reasons behind this are given in Section 1.1.

The analysis begins with the observation of deterioration, as compared to axisymmetric flow, in overall total pressure ratio and efficiency under distorted inlet flow (Section 4.1.1). Closer examination of the total pressure ratio and efficiency of the individual stages shows that this deterioration is due largely to the last 2 stages (Section 4.1.2). The particularly severe deterioration in total pressure ratio in these stages is associated with the manner in which the distortion travels from the far upstream boundary to the IGV inlet (Section 4.3) and then through the 11 stages (Section 4.4). These points will be elaborated upon in the following sections.

4.1 Results for Compressor Performance

4.1.1 Overall Performance

For the same corrected mass flow, the total pressure ratio and adiabatic efficiency of the whole compressor for each inlet condition is tabulated in Table 4.1.

Inlet Condition	Corrected Mass Flow (kg/s)	Total Pressure Ratio	Adiabatic Efficiency (%)
Axisymmetric	53.94	14.22	76.9
Distorted	53.94	10.35	71.8

Table 4.1 Compressor Performance for Axisymmetric and Distorted Inlet Flow

The compressor experiences a deterioration in total pressure ratio and efficiency as a result of inlet distortion. It will be shown in subsequent sections that the deterioration is associated with the behavior of a static pressure distortion which is eliminated over the last 2 stages.

The efficiency data in Table 4.1 is computed using total pressure and total temperature ratios. To assess the consistency of the computed efficiencies, these are calculated by using another approach that involves the losses generated by the body force representation and the increase in entropy across gaps between blade rows.

As losses can be quantified by increase in entropy, it is useful to relate the efficiency of a compressor to the increase in entropy according to the following equation

$$\eta = \frac{\pi^{\gamma-1/\gamma} - 1}{\left(\pi e^{\Delta s/R}\right)^{\gamma-1/\gamma} - 1} \tag{4.1}$$

where π is the total pressure ratio of the compressor.

In the body force representation, losses are generated in blade rows through the dissipative work term $\vec{F}_p \cdot \vec{V}_{rel}$, where $\vec{F}_p$ is the force component in the direction of the relative velocity $\vec{V}_{rel}$ [13,23]. This can be used to calculate the entropy increase due to the 23 blade rows. The rate of entropy generation for each blade row is calculated by a summation over the finite volume cells and is given by

$$\dot{S}_b = \sum_{cells} \frac{\vec{F}_p \cdot \vec{V}_{rel}}{T} \tag{4.2}$$

The change in entropy per unit mass across the blade row, Δs_b, is determined from an entropy balance.

$$\Delta s_b = \frac{\dot{S}_b}{\dot{m}} \tag{4.3}$$

The total change in entropy of the 23 blade rows is given by

$$\Delta s_{bt} = \sum_{\substack{blade \\ rows}} \Delta s_b \tag{4.4}$$

For gaps between blade rows, the entropy increase across each gap is determined from

$$\Delta s_g = c_p \ln \tau_g - R \ln \pi_g \tag{4.5}$$

where τ_g and π_g are static temperature and static pressure ratios across the gap respectively. The total change in entropy of the 22 gaps is given by

$$\Delta s_{gt} = \sum_{gaps} \Delta s_g \tag{4.6}$$

To separate the effects of blade rows and gaps on efficiency, the efficiency is first calculated from Eq. (4.1) using $\Delta s = \Delta s_{bt}$ (blade rows only) and then using $\Delta s = \Delta s_{bt} + \Delta s_{gt}$ (blade rows and gaps). The results for each inlet condition are tabulated in Table 4.2

Inlet Condition	**η (Blade Rows Only)**	**η (Blade Rows and Gaps)**	**Δη Due to Gaps**
Clean	78.2%	76.6%	1.6%
Distorted	73.7%	71.4%	2.3%

Table 4.2 Adiabatic Efficiency Calculated from Losses in Blade Rows and Gaps

The data of Table 4.2 demonstrates that the effects of gaps can be significant in a compressor with a large number of gaps (22 in the case of the 11-stage compressor) in which numerical dissipations occur. The larger decrement in calculated efficiency of 2.3% for distorted flow (as shown in the far right column of Table 4.2) as compared to 1.6% for clean flow could be due to numerical dissipation in the circumferential direction. The contribution from numerical dissipation in principle can be quantified through implementation of additional calculations with varying degrees of grid resolution and through extrapolation of the computed results. However, this has not been done here.

Another source of loss is the numerical dissipation within the blade rows. This has not been accounted for here. Hence it cannot be concluded that the computed efficiencies are self consistent.

The calculated distribution of entropy rise across the stages for clean and distorted inlet flow conditions is shown in Figs. 4.1(a) and (b) respectively. Entropy rise is defined non-dimensionally as $\frac{T_{ref}\Delta s}{U_{ref}^2}$. It is observed that for rotors, losses are highest for the first and last stages. For stators, losses are highest for the first stage. The entropy rise across gaps is highest at the last stage.

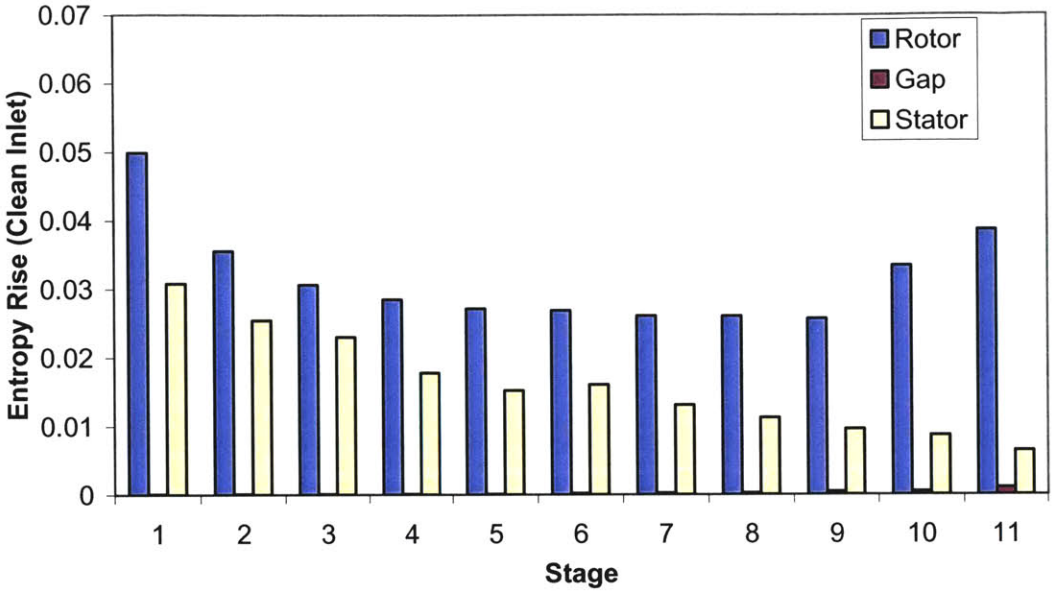

(a)

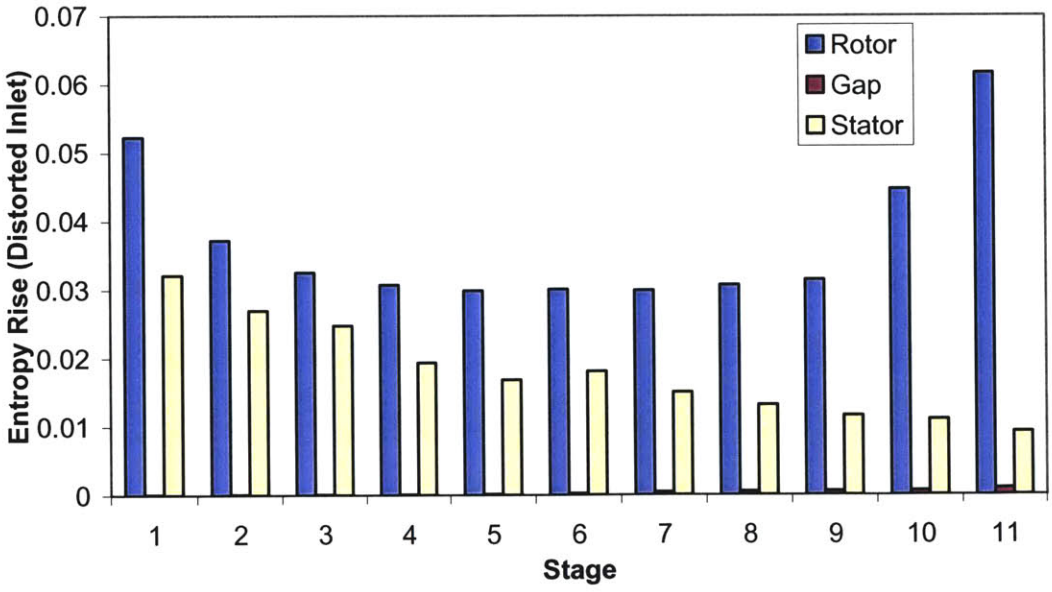

(b)

Fig. 4.1 Distribution of Entropy Rise Across the Stages for (a) Clean Inlet Flow

(b) Distorted Inlet Flow

4.1.2 Stage Performance

For distorted flow, the deterioration in total pressure ratio over the clean flow condition is calculated in each of the 11 stages and presented in Fig. 4.2. This deterioration is defined by the ratio $\frac{\pi_{clean} - \pi_{distorted}}{\pi_{ave} - 1}$, where π_{clean} and $\pi_{distorted}$ are stage total pressure ratios for the clean and distorted inlet conditions respectively. π_{ave} is the average stage total pressure ratio for the 11 stages. The deterioration can be seen to be particularly severe in the last 2 stages.

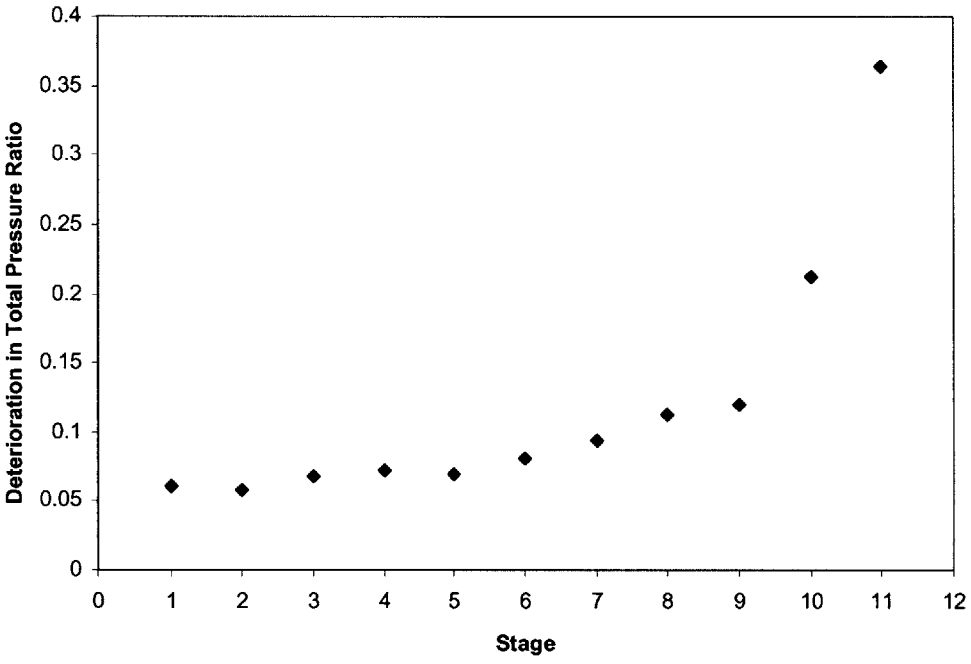

Fig. 4.2 Deterioration in Stage Total Pressure Ratio

The percentage decrease in efficiency, defined as $\left(\frac{\eta_{clean} - \eta_{distorted}}{\eta_{clean}}\right) \times 100\%$, for each stage is shown in Fig. 4.3. The deterioration in efficiency is found to be most severe also in the last 2 stages.

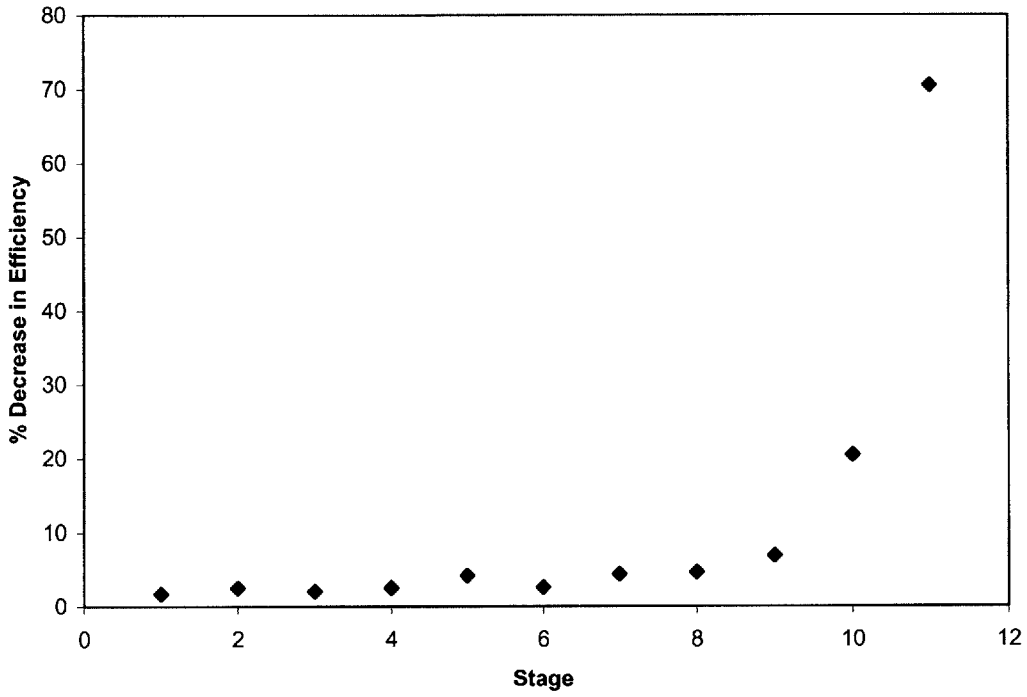

Fig. 4.3 Deterioration in Efficiency

It can be seen from the data of Figs. 4.2 and 4.3 that, although the same computational model (Eqns. (2.2) to (2.5)) is used in all the stages to compute the body forces from local flow conditions, inlet distortion produces varying degrees of performance deterioration among the stages. Certain stages are found to be insensitive to inlet distortion as compared to other stages (for example, from Figs. 4.2 and 4.3, the first 3 stages are insensitive to inlet distortion as compared to the last 2 stages). This suggests, hypothetically, that it may be possible to design a compressor that is insensitive to inlet

distortion by modifying Eqns. (2.2) to (2.5) (which already produce robustness for certain stages) to produce robustness for each stage. The resulting body force representation can then be used to determine the blade geometry of a compressor whose performance does not deteriorate significantly with inlet distortion.

The particularly severe deterioration in performance in the last two stages is associated with the formation of a static pressure distortion at the IGV inlet (Section 4.3), its amplification through the first 9 stages (Section 4.4.1) and its abrupt elimination through the final 2 stages (Section 4.4.2). These will be described in the following sections as part of an analysis of the computed flow field. The physical consistency of the computed flow field will also be assessed as a means of demonstrating the utility of the body force representation for inlet distortion computations.

4.2 Static Pressure at Compressor Outlet

The static pressure at the compressor outlet has an important effect on the manner in which the inlet distortion propagates from the upstream boundary and through the compressor. In the absence of coupling with nozzles or diffusers, this is expected to be circumferentially uniform [16,19,22].

The computed mid-radius static pressure (defined as P/P_{ref} where P_{ref} is reference pressure, selected to be the total pressure at the upstream boundary. Plots of static pressure will use this definition hereon) at the compressor exit is shown in Fig. 4.4 and is examined for consistency with the condition of circumferential uniformity before

beginning an analysis of the propagation of the distortion. This can be seen to be uniform circumferentially and is consistent with the expected result, with the implication that further examination of the computed flow field can be proceeded with.

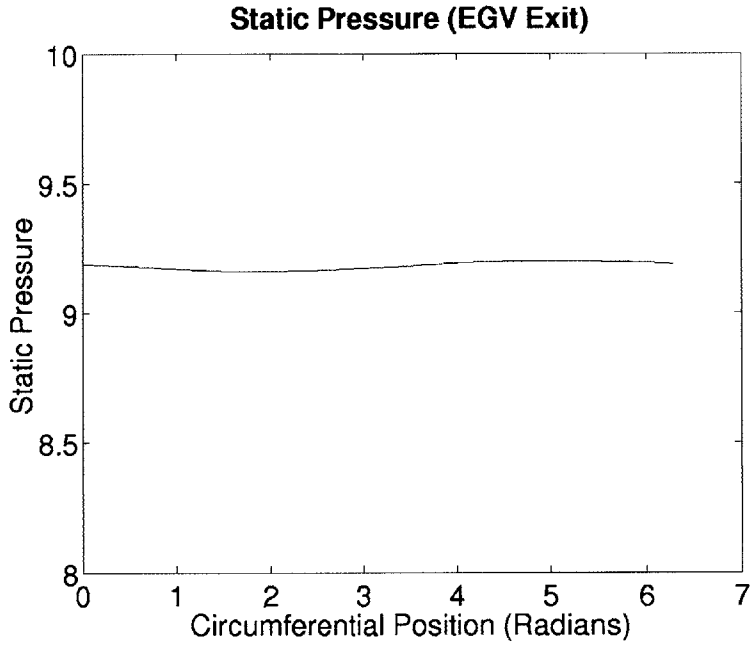

Fig. 4.4 Computed Mid-radius Static Pressure at Compressor Exit

4.3 Distortion Behavior from Upstream Boundary to IGV Inlet

Two essential phenomena will be analyzed for consistency in this section. The first phenomena is the formation of a static pressure distortion at the IGV inlet. This gives rise to changes in the velocity distortion and the circumferential extent of the low total pressure section of the distortion, as well as an induced swirl. The second one is the asymmetric character of the velocity distortion at the IGV inlet. This asymmetric distribution is discussed in terms of the momentum transport effects of rotors [19].

4.3.1 Formation of Static Pressure Distortion at IGV Inlet

The change in circumferential extent of the low total pressure section can be explained by first considering the result presented previously in Section 4.2, that static pressure is uniform at the compressor exit. Also, in compressors, the variation of static pressure rise ψ (defined as $\frac{\Delta P_s}{\frac{1}{2}\rho U^2}$) with flow coefficient ϕ follows a decreasing trend as shown in Fig. 4.5.

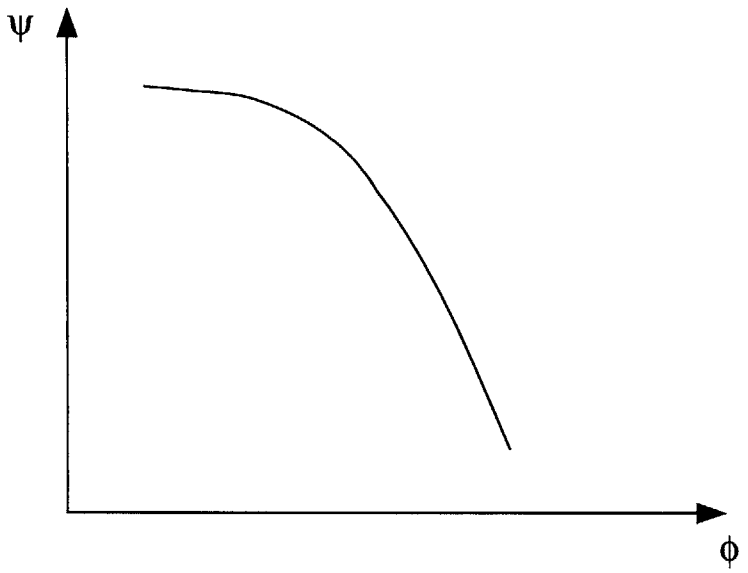

Fig. 4.5 Variation of Pressure Rise with Flow Coefficient

The region of lower flow in the distortion corresponds to higher loading, and hence static pressure there is reduced as the inlet distortion travels from the upstream boundary (where static pressure is circumferentially uniform) to the IGV inlet, leading to a static pressure distortion at the IGV inlet. The reduction in static pressure also leads to an increase in velocity (conversely, the static pressure and velocity in the high total pressure region are increased and decreased respectively), leading to an attenuation of the velocity

distortion at the IGV inlet. By continuity and knowing that total pressure is convected with streamlines, the circumferential extent of the low total pressure region is expected to be reduced as it travels towards the IGV inlet, giving rise to an induced swirl.

The computed flow field is examined for consistency with the expected flow features. The computed mid-radius static pressure at the IGV inlet as shown in Fig. 4.6 indicates that a static pressure distortion does indeed form at the IGV inlet. The computations also reveal the associated attenuation in the velocity distortion as shown in Fig. 4.7 which are plots of the mid-radius flow coefficient at the upstream boundary (Fig. 4.7(a)) and IGV inlet (Fig. 4.7(b)). The computed mid-radius total pressures (defined as P_t/P_{ref} where P_{ref} is reference pressure, selected to be the total pressure at the upstream boundary) at the upstream boundary and the IGV inlet show consistency with the expected reduction in circumferential extent of the low total pressure region, as indicated in Fig. 4.8. Finally, the existence of an induced swirl can be seen from the plot of mid-radius flow angles at the IGV inlet, as shown in Fig. 4.9.

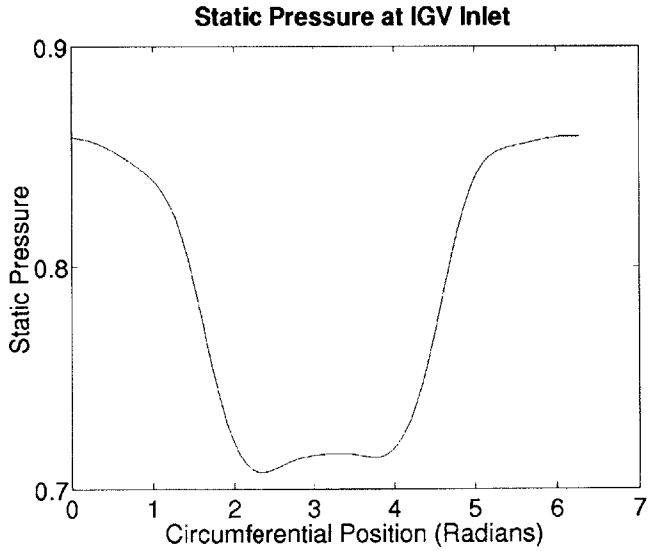

Fig. 4.6 Static Pressure Distortion at the Mid-radius of the IGV Inlet

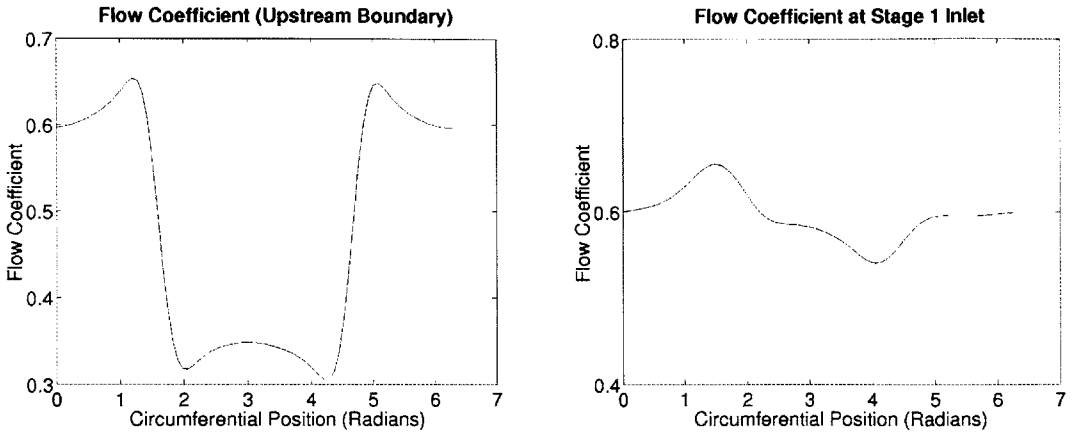

(a) (b)

Fig. 4.7 Mid-radius Velocity Distributions at (a) Upstream Boundary and (b) IGV Inlet, Showing Attenuation of the Velocity Distortion at the IGV Inlet

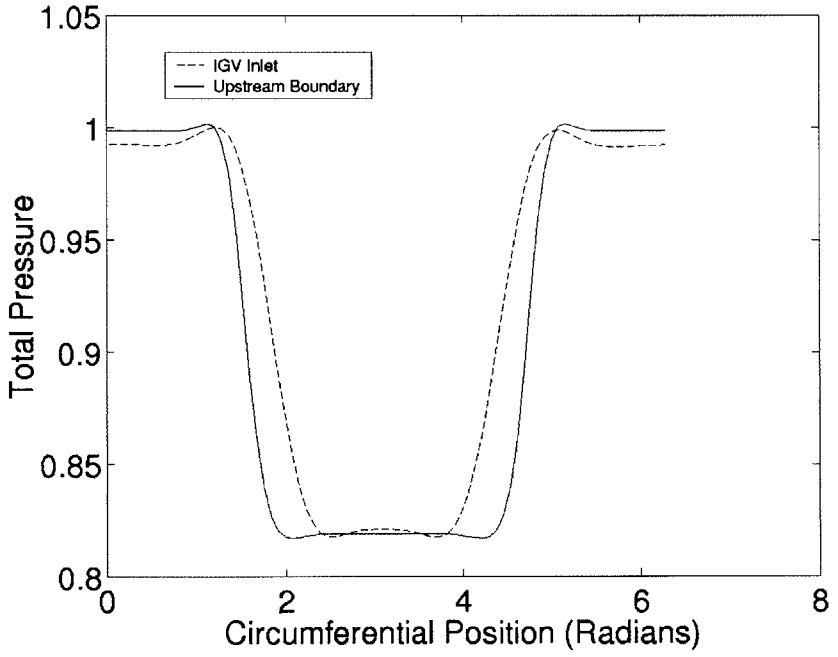

Fig. 4.8 Total Pressure at Mid-Radius of the IGV Inlet, Showing Reduction of Circumferential Extent of Low Total Pressure Region from Upstream Boundary to IGV Inlet

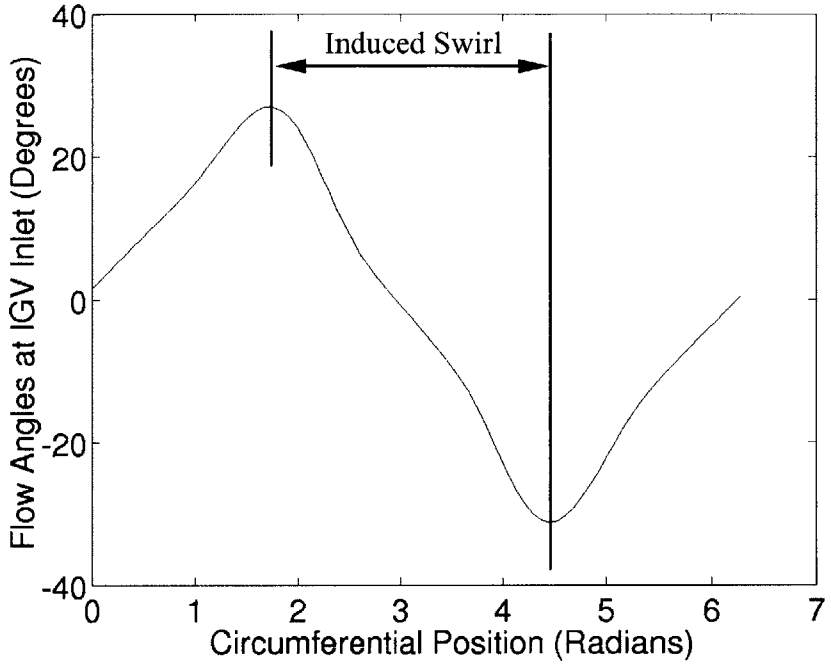

Fig. 4.9 Flow Angles at IGV Inlet, Showing Induced Swirl

4.3.2 Asymmetric Character of the Velocity Distortion at the IGV Inlet

To further analyze the physical consistency of the computed flow field, the asymmetric nature of the velocity distortion as shown in Fig. 4.7(b) is examined. The factor that is taken into consideration is the transport of momentum brought about by rotor rotation. This effect has been incorporated in the actuator disk model of Hynes and Greitzer [19] and is responsible for the shift in the minimum peak of the velocity distortion in their computations. For the present computations, the trend of the computed asymmetric velocity distortion agrees with that of Hynes and Greitzer [19], with the minimum peak shifted in the same direction as that of Ref. [19], as shown in Fig. 4.7(b).

To summarize, up to this point, the following have been analyzed for consistency:

- Adiabatic efficiency
- Circumferentially uniform static pressure at the compressor exit (Fig. 4.4)
- Formation of a static pressure distortion at the IGV inlet (Fig. 4.6). Associated with this is the attenuation in the velocity distortion (Fig. 4.7), the reduction in circumferential extent of the low total pressure region (Fig. 4.8) and the induced swirl (Fig. 4.9)
- Asymmetric nature of the velocity distortion at the IGV inlet (Fig. 4.7(b))

4.4 Distortion Propagation Through Compressor Stages

Having established the occurrence of a static pressure distortion at the IGV inlet, this section examines its propagation through the compressor stages. The manner in which the propagation occurs will lead to an understanding as to why deterioration in total pressure ratio is particularly significant in the last 2 stages as compared to the other stages (Fig. 4.1).

The key features of the propagation of the static pressure distortion are

- Amplification through the first 9 stages
- Strong attenuation within the last 2 stages, resulting in circumferentially uniform variation at the compressor exit. It will be shown that this takes place in a manner which results in severe deterioration in total pressure ratio.

These features are illustrated in Fig. 4.10 which shows the mid-radius static pressure range at the inlet of each stage and will be further described in Sections 4.4.1 and 4.4.2.

Static pressure range is defined as $\frac{P_{max} - P_{min}}{\frac{1}{2}\rho U^2}$ at the mid-radius and is used here as a measure of the severity of distortion.

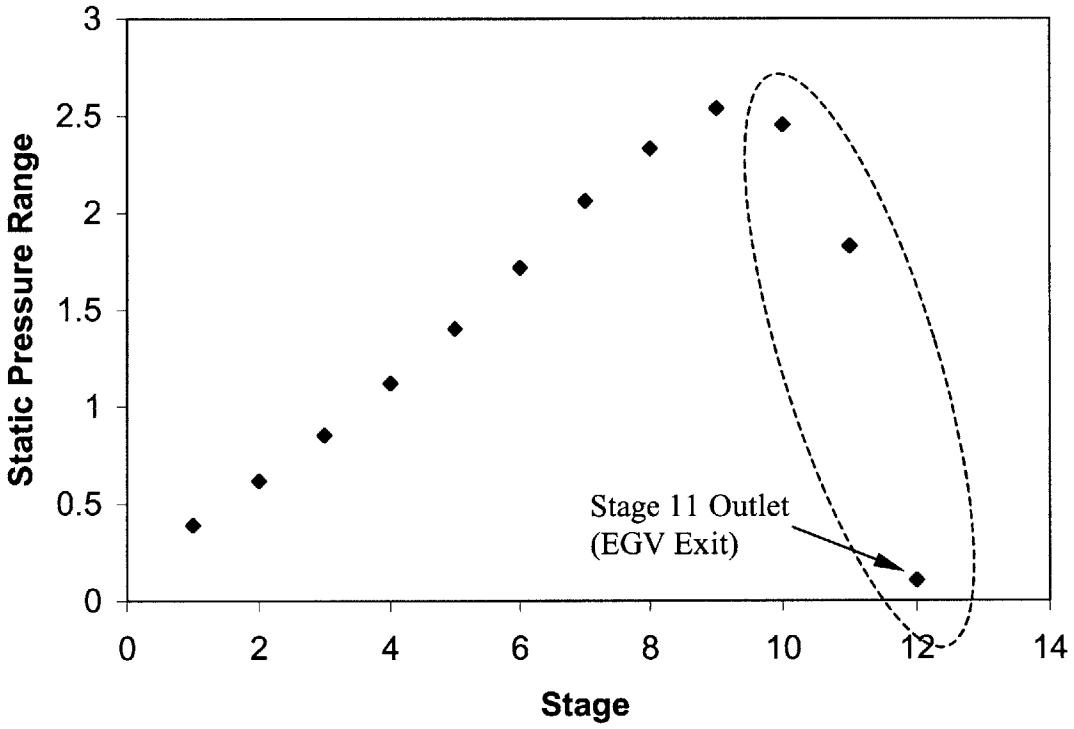

Fig. 4.10 Range of Static Pressure for Each Stage, with the Circled Region Showing Strong Attenuation in Static Pressure Distortion Across the Last 2 Stages

4.4.1 Amplification of Static Pressure Distortion Through First 9 Stages

The amplification effect of the static pressure distortion is observed, from inspection of data at various axial locations as shown in Fig. 4.11, to occur through the first 9 stages.

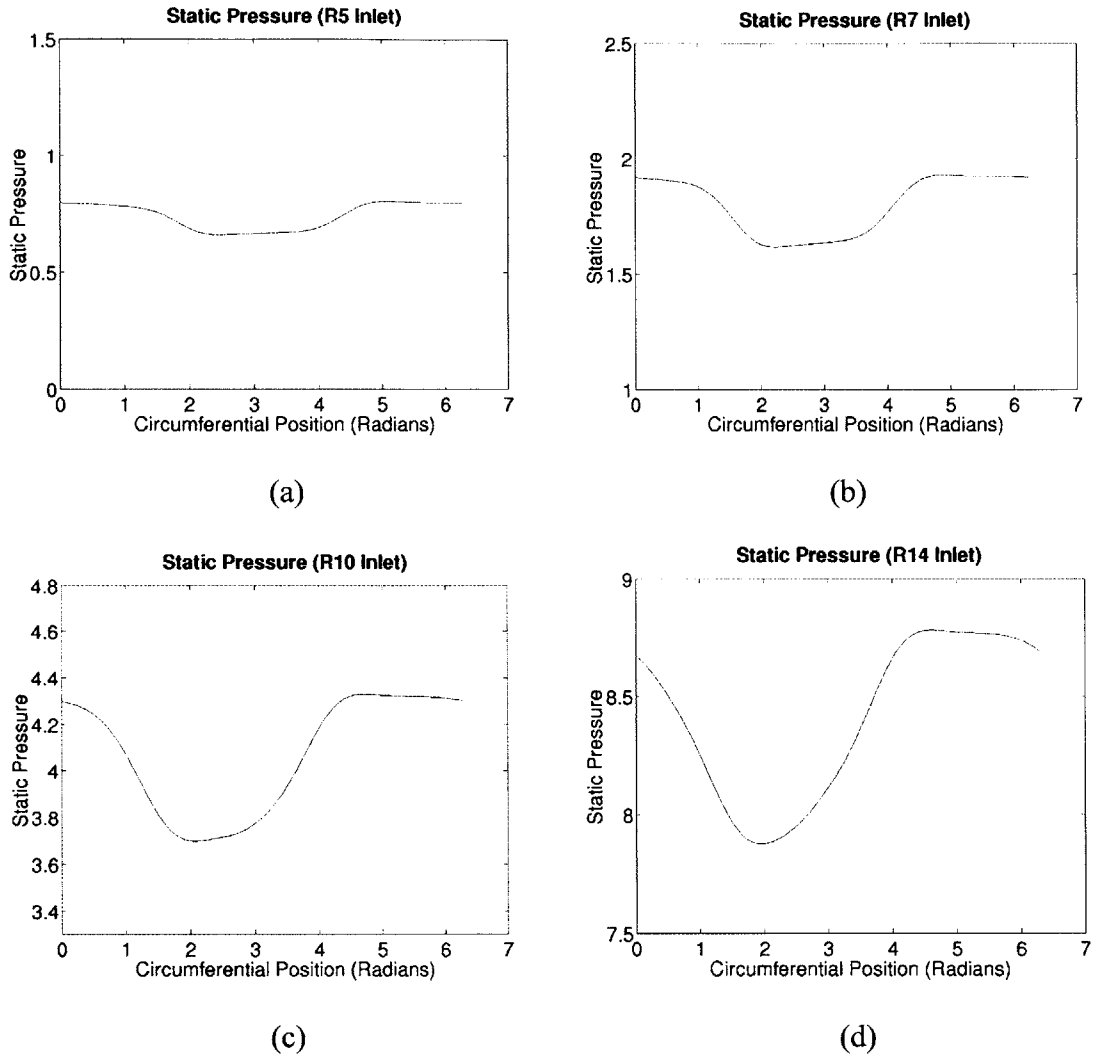

Fig. 4.11 Amplification of Static Pressure Distortion, as Shown by Mid-radius Static Pressure at (a)Stage 1 Inlet, (b)Stage 3 Inlet, (c) Stage 5 Outlet and (d)Stage 9 Outlet

4.4.2 Attenuation of Static Pressure Distortion Through Last 2 Stages

The static pressure distortion cannot be amplified throughout the compressor, but must be attenuated at some stage since the condition of uniform static pressure at the compressor exit must be satisfied. The attenuation is achieved in the last 2 stages, most noticeably in the last stage (stage 11), as shown in Fig. 4.12 which shows the pressure distortion at

mid-radius being abruptly eliminated, resulting in a uniform distribution at the compressor exit (stage 11 outlet).

Closer examination of Fig. 4.12 shows that the elimination of the distortion involves static pressure reduction in certain areas. The total pressure also falls in these areas, as shown in Fig. 4.13 which plots P_t/P_{ref}. Upon examining the mass-averaged total pressure rise across each of the 11 stages as shown in Fig. 4.14, it is found that the mass-averaged total pressure actually falls across stage 11, resulting in the severe deterioration in total pressure ratio over the clean inlet condition, as observed previously in Fig. 4.1. It is uncertain as to how the number of stages over which amplification or attenuation takes place could be determined. Future work in this area is recommended.

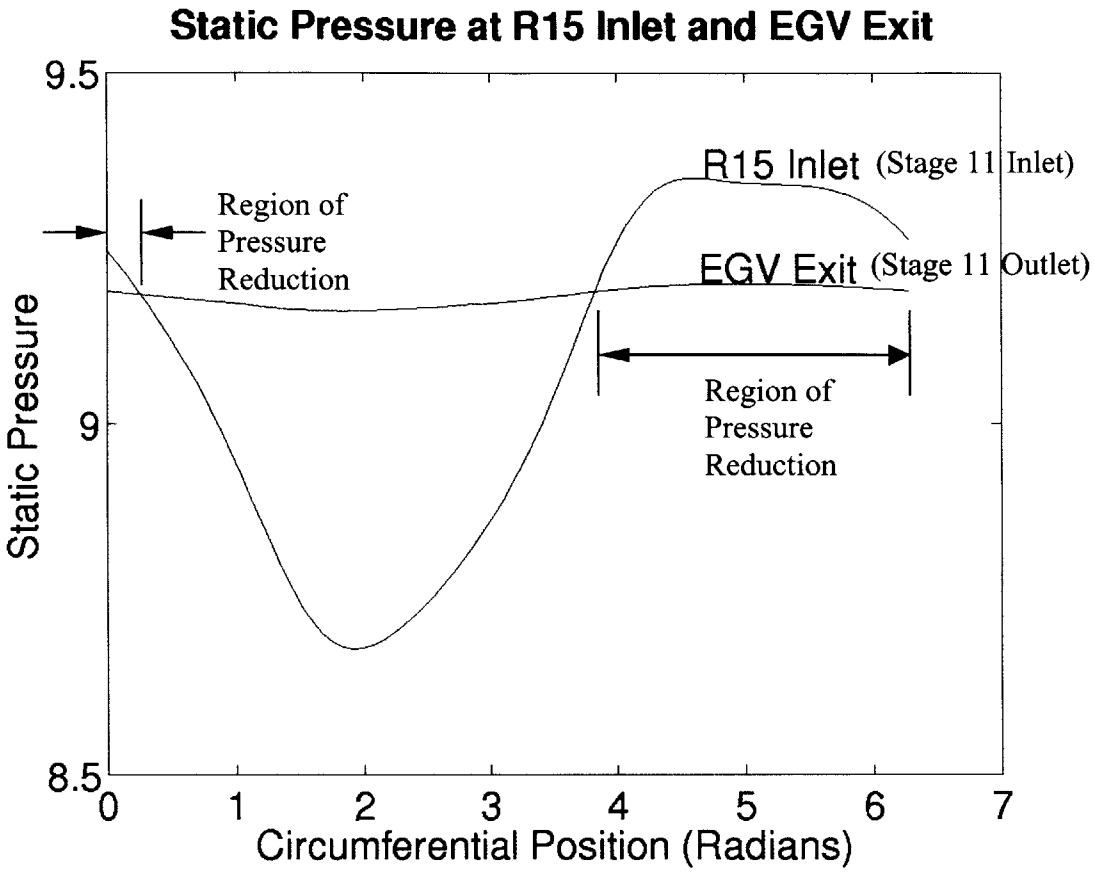

Fig. 4.12 Elimination of Static Pressure Distortion Across Stage 11, Showing Regions in which Pressure is Reduced

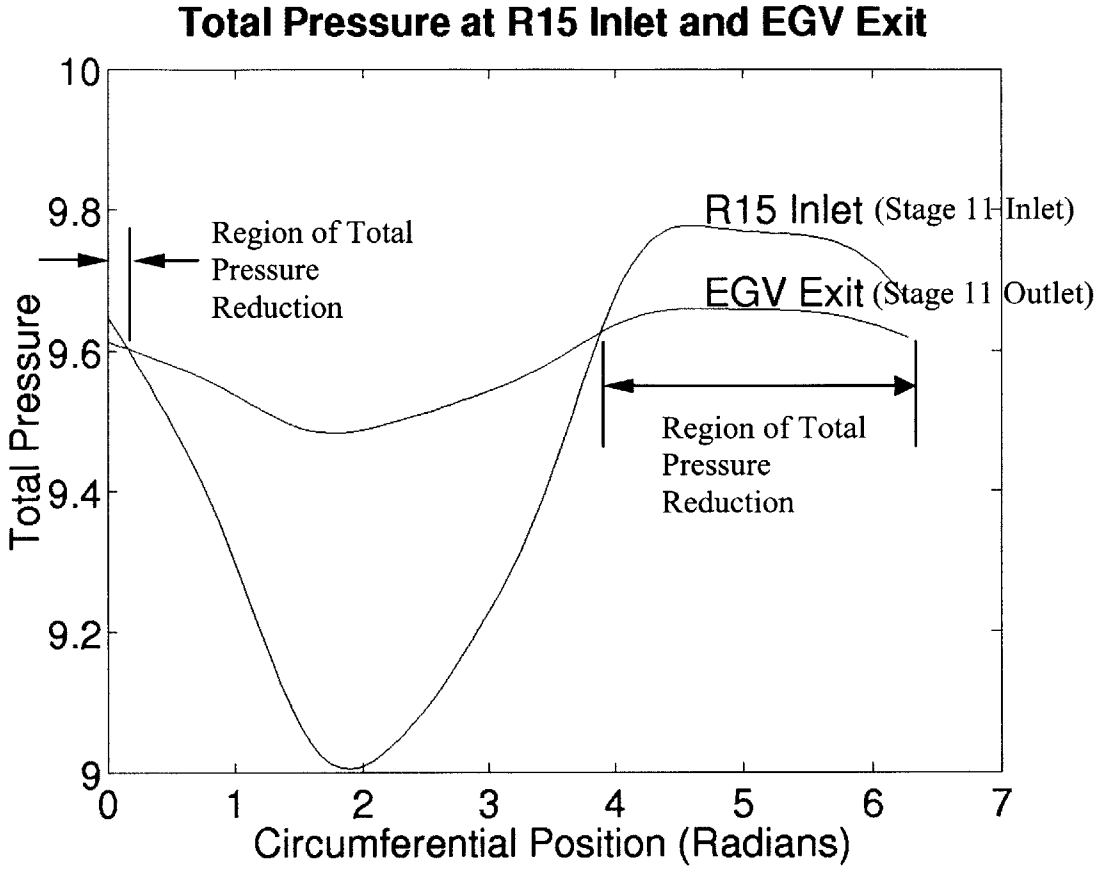

Fig. 4.13 Total Pressure at R15 Inlet and EGV Exit (Stage 11 Inlet and Outlet Respectively), Showing Regions in which Total Pressure is Reduced

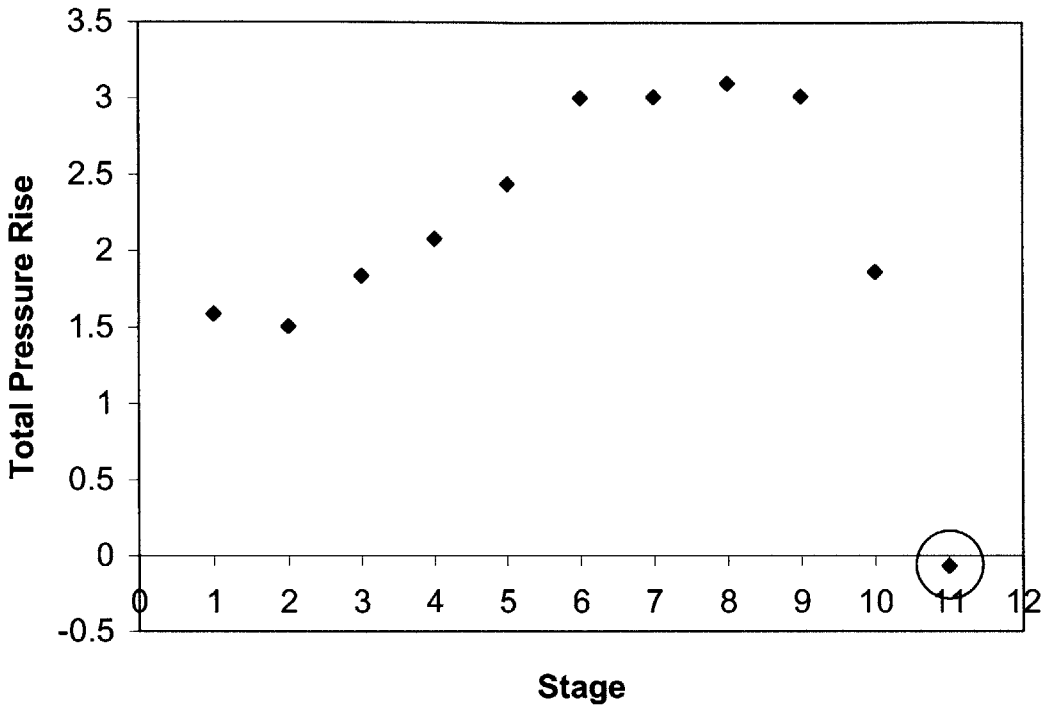

Fig. 4.14 Total Pressure Rise Across Each Stage, Showing that Total Pressure Actually Falls Across Stage 11 (Circled). Total Pressure Rise for a Stage is Defined as $\frac{P_{t,outlet} - P_{t,inlet}}{\frac{1}{2}\rho U^2}$

4.5 Chapter Summary

Results for inlet distortion computations have been presented in this chapter. The deterioration in performance has been predicted and is found to be particularly severe in the last 2 stages. This is found through an analysis of the flow field to be associated with the behavior of a static pressure distortion which forms at the IGV inlet, is amplified through the first 9 stages and then abruptly eliminated through the last 2 stages.

To demonstrate the utility of the body force representation for inlet distortion computations, the performance and flow field are also analyzed for consistency. The analysis is performed on the following:

- Adiabatic efficiency
- Circumferentially uniform static pressure at the compressor exit
- Formation of a static pressure distortion at the IGV inlet. Associated with this is the attenuation in velocity distortion, the reduction in circumferential extent of the low total pressure region and the induced swirl
- Asymmetric nature of the velocity distortion at the IGV inlet

CHAPTER 5 : SUMMARY, CONCLUSIONS AND FUTURE WORK

5.1 Summary

The thesis presents the formulation of a blade-row-by-blade-row body force representation of an 11-stage compressor based on streamline curvature data. The applicability of such a representation is assessed in axisymmetric flow computations. The utility of using body forces to compute the response of a high-speed multistage compressor to inlet distortion is also assessed. The computed performance and flow field are analyzed for consistency.

In Chapter 1, that blade row effects of pressure rise, flow turning and energy exchanges can be replaced by a body force field is presented. The method of deriving the blade-row-by-blade-row body force representation of a multistage compressor from streamline curvature data is proposed. This approach is rigorous and more computationally efficient than using Navier-Stokes solver. The objectives are stated, and involve assessing the applicability of such a body force representation.

Chapter 2 presents the governing equations for the body force representation and that this is equivalent to the infinite number of blades model of a blade row. Such a model is adequate for assessing compressor response to circumferential flow non-uniformity of length scale larger than a blade pitch. The implementation of the methodology for axisymmetric and inlet distortion computations on an 11-stage compressor is presented.

In Chapter 3, through an analysis of results from axisymmetric computations, assessment is made of the applicability of the body force representation extracted from streamline curvature data. The total pressure ratio is found to be in 2.3% agreement with the reference streamline curvature data.

In Chapter 4, the utility of the body force representation for computing compressor response to inlet distortion is assessed. The performance and flow field are analyzed for consistency. The following features are involved in the analysis:

- Adiabatic efficiency
- Circumferentially uniform static pressure at the compressor exit
- Formation of a static pressure distortion at the IGV inlet. Associated with this is the attenuation in the velocity distortion, the reduction in circumferential extent of the low total pressure region and the induced swirl
- Asymmetric nature of the velocity distortion at the IGV inlet

The particularly severe deterioration in performance in the last two stages is associated with the formation of a static pressure distortion at the IGV inlet, its amplification through the first 9 stages and its elimination through the final 2 stages.

5.2 Conclusions

The following conclusions have been deduced from the computational results:

1. The blade-row-by-blade-row body force representation of a multistage compressor can be derived from streamline curvature data at low computational expense (advantageous over using Navier-Stokes data). However, the representation is limited by the streamline curvature data's use of correlations to account for losses. The representation has been analyzed for consistency but further application for computing compressor response to inlet distortion has not been implemented.
2. The use of the body force formulation of Gong [13] to compute, for an 11-stage compressor, (1) performance and flow field under clean inlet conditions and (2) the response to inlet distortion at the same corrected mass flow, yields a decrement in efficiency (using total pressure and total temperature ratios) of 5 % due to inlet distortion. By considering losses generated within blade rows, the decrement is 4.5%. The discrepancy of 0.5% can be accounted for by numerical dissipation in the gaps between blade rows and the blade rows themselves. The latter has not been considered.

5.3 Recommendations for Future Work

Two central issues pertaining to inlet distortion are:

1. Predicting the deteriorated performance and stall margin
2. Developing improved compressor designs or strategies to minimize the deterioration in performance and stability.

The following work would enable further insight on the behavior of multistage compressors under inlet distortion to be gained, and could lead to design strategies for engines which are insensitive to a wide variety of distortion profiles:

1. Developing an improved computational model for simulating compressor operation. In this work, the model, as described in Section 2.6, for calculating the body force coefficients K_n and K_p may not be adequately representative of the compressor. It is recommended that these be obtained from the reference streamline curvature data or, if available, experimental or Navier-Stokes results.
2. With an improved model, further investigations of compressor performance under various types of inlet distortions could be performed. These would include total pressure or total temperature distortions of various circumferential extents, or even transient distortions.
3. Having hypothesized that it is possible to devise a body force model specifically for each stage, such that the resulting compressor's performance is insensitive to inlet distortion (as presented in Section 4.2), it would be fruitful to formulate techniques to determine such a body force representation, and then use the representation to determine the blade geometry.

APPENDIX A : DERIVATION OF GOVERNING EQUATIONS

In this appendix, the governing equations for through-flow calculations are derived. These are essentially the Euler equations in terms of pitch-wise averaged quantities. Blade row effects are represented by body forces, a technique previously used and described in Refs. [2,7,18,23].

The general principle used in the derivation of the governing equations is that a general 3-dimensional flow field of an axial turbomachine can be reduced to an axisymmetric flow field with body forces [18]. The method for deriving the equations is as follows. Starting with the 3-dimensional Navier-Stokes equations, these are averaged in the circumferential direction. The resulting equations thus obtained contain pitch-wise averaged flow variables, as well as additional terms due to blade geometry and viscous forces. These additional terms are re-expressed as body forces.

A.1 Derivation of Governing Equations

The 3-dimensional unsteady Navier-Stokes equations in cylindrical coordinates with no heat generation are given by

$$\frac{\partial U}{\partial t}+\frac{\partial F_{inv}}{\partial x}+\frac{\partial G_{inv}}{\partial \theta}+\frac{\partial H_{inv}}{\partial r}=S+\frac{\partial F_{vis}}{\partial x}+\frac{\partial G_{vis}}{\partial \theta}+\frac{\partial H_{vis}}{\partial r} \qquad \text{(A.1)}$$

$$\text{where } U = \begin{vmatrix} r\rho \\ r\rho V_x \\ r\rho V_\theta \\ r\rho V_r \\ r\rho e_t \end{vmatrix},\ F_{inv} = \begin{vmatrix} r\rho V_x \\ r\left(\rho V_x{}^2 + p\right) \\ r\rho V_x V_\theta \\ r\rho V_x V_r \\ rV_x(\rho e_t + p) \end{vmatrix},\ G_{inv} = \begin{vmatrix} \rho V_\theta \\ \rho V_x V_\theta \\ \rho V_\vartheta{}^2 + p \\ \rho V_\theta V_r \\ V_\theta(\rho e_t + p) \end{vmatrix},\ H_{inv} = \begin{vmatrix} r\rho V_r \\ r\rho V_x V_r \\ r\rho V_\theta V_r \\ r\left(\rho V_r{}^2 + p\right) \\ rV_r(\rho e_t + p) \end{vmatrix},$$

$$S = \begin{vmatrix} 0 \\ 0 \\ -\rho V_\theta V_r \\ \rho V_\theta{}^2 + p \\ 0 \end{vmatrix},\ F_{vis} = \begin{vmatrix} 0 \\ r\tau_{xx} \\ r\tau_{x\theta} \\ r\tau_{xr} \\ r\left(V_r\tau_{xr} + V_\theta\tau_{x\theta} + V_x\tau_{xx}\right) \end{vmatrix},\ G_{vis} = \begin{vmatrix} 0 \\ \tau_{\theta x} \\ \tau_{\theta\theta} \\ \tau_{\theta r} \\ V_r\tau_{\theta r} + V_\theta\tau_{\theta\theta} + V_x\tau_{\theta x} \end{vmatrix},$$

$$H_{vis} = \begin{vmatrix} 0 \\ r\tau_{rx} \\ r\tau_{r\theta} \\ r\tau_{rr} \\ r\left(V_r\tau_{rr} + V_\theta\tau_{r\theta} + V_x\tau_{xr}\right) \end{vmatrix}$$

Define pitch-wise average of a quantity q as

$$\bar{q} = \frac{1}{\Delta\theta}\int_{\theta_1}^{\theta_2} q \quad d\theta$$

where the integral is taken through a circular arc path which runs across the blade passage as illustrated in Fig. A.1. $\Delta\theta = \theta_2 - \theta_1$

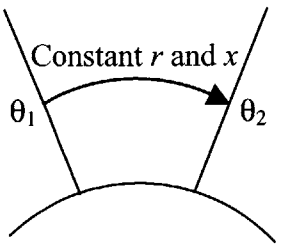

Fig. A.1

The Navier-Stokes equations as given by Eq. (A.1) are integrated across a circular path, as shown in Fig. A.1, to obtain equations in the x-r meridional plane in terms of pitch-wise averaged flow quantities (e.g. $\bar{\rho}$, $\bar{p}$ etc.). Upon obtaining the pitchwise averaged equations, body force terms which represent blade row effects are identified, and some physical aspects of these forces can be deduced.

The integration of the Navier-Stokes equations, Eqn. (A.1), will involve the integration of x-derivative and r-derivative terms. An important relation that is used in the integration of x-derivative terms in the Navier-Stokes equations is

$$\int_{\theta_1}^{\theta_2} \frac{\partial q}{\partial x} d\theta = \frac{\partial}{\partial x}\left(\bar{q}\Delta\theta\right) + q_{\theta_1}\frac{\partial \theta_1}{\partial x} - q_{\theta_2}\frac{\partial \theta_2}{\partial x} \tag{A.2}$$

From Eqn. (A.2), it can be seen that the integration of an x-derivative term produces the averaged quantity $\bar{q}$. Quite importantly, additional terms which are dependent on blade geometry ($\frac{\partial \theta_1}{\partial x}$ and $\frac{\partial \theta_2}{\partial x}$) and boundary values ($q_{\theta_1}$ and q_{θ_2}) are also produced. The reason for the presence of blade geometry terms is that the curvature of the blade surfaces causes the limits of integration, θ_1 and θ_2, to change with x.

Similarly, integration of r-derivative terms in the Navier-Stokes equations follows the relation

$$\int_{\theta_1}^{\theta_2} \frac{\partial q}{\partial r} d\theta = \frac{\partial}{\partial r}\left(\bar{q}\Delta\theta\right) + q_{\theta_1}\frac{\partial \theta_1}{\partial r} - q_{\theta_2}\frac{\partial \theta_2}{\partial r} \tag{A.3}$$

Again, terms dependent on blade geometry and boundary values are present.

An assumption is made with regard to neglecting other terms which emerge upon integration. Suppose 2 flow quantities ϕ and ψ along the path of integration can be expressed as $\Phi + \phi'$ and $\Psi + \psi'$ (sum of mean and fluctuation terms), then

$$\overline{\phi\psi} = \Phi\Psi + \overline{\phi'\psi'}$$

Terms involving products of fluctuations are assumed small.

Upon integration of the 3-dimensional Navier-Stokes equations given by Eq. (A.1), the resulting equations have the following form:

$$\frac{\partial(b\overline{U})}{\partial t} + \frac{\partial(b\overline{F}_{inv})}{\partial x} + \frac{\partial(b\overline{H}_{inv})}{\partial r} = b\overline{S} + K_{inv} + K_{vis} + \frac{\partial(b\overline{F}_{vis})}{\partial x} + \frac{\partial(b\overline{H}_{vis})}{\partial r} \qquad \text{(A.4)}$$

where b is a blockage factor, defined by

$$b = \frac{\Delta\theta}{\Delta\theta_0}$$

$\Delta\theta_0$ is the angular pitch at the inlet of the flow passage as illustrated in Fig. A.2.

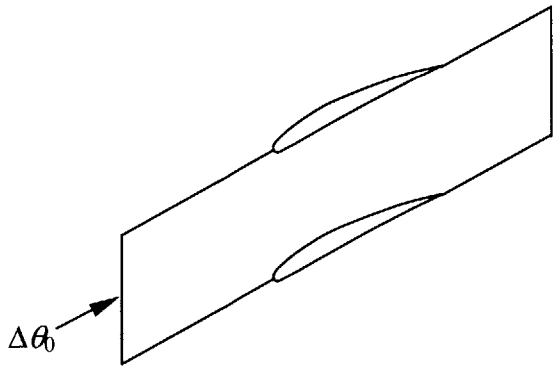

Fig. A.2 Definition of $\Delta\theta_0$

K_{inv} and K_{vis} contain boundary values and geometric terms for the inviscid and viscous fluxes respectively. $\overline{U}$, $\overline{F}$ and $\overline{H}$ can be constructed from pitchwise averages of the various flow quantities (e.g. $\overline{\rho}$, $\overline{p}$ etc.). For each of the conservation equations,

$$K_{inv} = \frac{1}{\Delta\theta_0}\left[\left(F_{inv,\theta_2}\frac{\partial\theta_2}{\partial x} - F_{inv,\theta_1}\frac{\partial\theta_1}{\partial x}\right) + \left(G_{inv,\theta_1} - G_{inv,\theta_2}\right) + \left(H_{inv,\theta_2}\frac{\partial\theta_2}{\partial r} - H_{inv,\theta_1}\frac{\partial\theta_1}{\partial r}\right)\right]$$

$$K_{vis} = \frac{1}{\Delta\theta_0}\left[\left(F_{vis,\theta_1}\frac{\partial\theta_1}{\partial x} - F_{vis,\theta_2}\frac{\partial\theta_2}{\partial x}\right) + \left(G_{vis,\theta_2} - G_{vis,\theta_1}\right) + \left(H_{vis,\theta_1}\frac{\partial\theta_1}{\partial r} - H_{vis,\theta_2}\frac{\partial\theta_2}{\partial r}\right)\right]$$

Defining

$$\Delta_1(\bullet) = (\bullet)_{\theta_2}\frac{\partial\theta_2}{\partial x} - (\bullet)_{\theta_1}\frac{\partial\theta_1}{\partial x}$$

$$\Delta_2(\bullet) = (\bullet)_{\theta_2} - (\bullet)_{\theta_1}$$

$$\Delta_3(\bullet) = (\bullet)_{\theta_2}\frac{\partial\theta_2}{\partial r} - (\bullet)_{\theta_1}\frac{\partial\theta_1}{\partial r}$$

then K_{inv} and K_{vis} may be expressed as

$$K_{inv} = \frac{1}{\Delta\theta_0}\begin{vmatrix} r\Delta_1(\rho V_x) - \Delta_2(\rho V_\theta) + r\Delta_3(\rho V_r) \\ \left[r\Delta_1\left(\rho V_x^{\,2}\right) + r\Delta_1(p)\right] - \Delta_2(\rho V_x V_\theta) + r\Delta_3(\rho V_x V_r) \\ r\Delta_1(\rho V_x V_\theta) - \left[\Delta_2\left(\rho V_\theta^{\,2}\right) + \Delta_2 p\right] + r\Delta_3(\rho V_\theta V_r) \\ r\Delta_1(\rho V_x V_r) - \Delta_2(\rho V_\theta V_r) + \left[r\Delta_3\left(\rho V_r^{\,2}\right) + r\Delta_3(p)\right] \\ r\left[\Delta_1(V_x\rho e_t) + \Delta_1(V_x p)\right] - \left[\Delta_2(V_\theta\rho e_t) + \Delta_2(V_\theta p)\right] + r\left[\Delta_3(V_r\rho e_t) + \Delta_3(V_r p)\right] \end{vmatrix} \quad \text{(A.5)}$$

$$K_{vis} = \frac{1}{\Delta\theta_0}\begin{vmatrix} 0 \\ -r\Delta_1(\tau_{xx}) + \Delta_2(\tau_{\theta x}) - r\Delta_3(\tau_{rx}) \\ -r\Delta_1(\tau_{x\theta}) + \Delta_2(\tau_{\theta\theta}) - r\Delta_3(\tau_{r\theta}) \\ -r\Delta_1(\tau_{xr}) + \Delta_2(\tau_{\theta r}) - r\Delta_3(\tau_{rr}) \\ \alpha_1 + \alpha_2 + \alpha_3 \end{vmatrix} \quad \text{(A.6)}$$

$$\alpha_1 = -r\left[\Delta_1(V_r\tau_{xr}) + \Delta_1(V_\theta\tau_{x\theta}) + \Delta_1(V_x\tau_{xx})\right]$$

$$\alpha_2 = [\Delta_2(V_r\tau_{\theta r}) + \Delta_2(V_\theta\tau_{\theta\theta}) + \Delta_2(V_x\tau_{\theta x})]$$

$$\alpha_1 = -r[\Delta_3(V_r\tau_{rr}) + \Delta_3(V_\theta\tau_{r\theta}) + \Delta_3(V_x\tau_{xr})]$$

In Eq. (A.4), the last 4 terms on the right-hand side may be grouped together into a "body force", such that the equation models a general 3-dimensional flow field in an axial turbomachine as an axisymmetric flow field with body forces [18]. The equation with body forces is written as

$$\frac{\partial(b\overline{U})}{\partial t} + \frac{\partial(b\overline{F}_{inv})}{\partial x} + \frac{\partial(b\overline{H}_{inv})}{\partial r} = b\overline{S} + \overline{F} \tag{A.7}$$

where $\overline{F} = \begin{vmatrix} 0 \\ r\overline{\rho}f_x \\ r\overline{\rho}f_\theta \\ r\overline{\rho}f_r \\ r\overline{\rho}(\vec{f}\cdot\vec{V}) \end{vmatrix}$

$\vec{f}$ is the body force per unit mass with components f_x, f_θ and f_r. $\vec{V}$ is the velocity vector.

A.2 Body Forces and their Physical Significance

Within the blade passage (except for the leading and trailing edges), $\frac{\partial\theta_1}{\partial x} \approx \frac{\partial\theta_2}{\partial x} = \frac{\partial\theta}{\partial x}$ and $\frac{\partial\theta_1}{\partial r} \approx \frac{\partial\theta_2}{\partial r} = \frac{\partial\theta}{\partial r}$. Due to no-slip conditions, for a stator,

$$K_{inv} \approx \frac{1}{\Delta\theta_0}\begin{vmatrix} 0 \\ r\Delta_2(p)\frac{\partial\theta}{\partial x} \\ -\Delta_2 p \\ r\Delta_2(p)\frac{\partial\theta}{\partial r} \\ 0 \end{vmatrix} \tag{A.8}$$

$$K_{vis} \approx \frac{1}{\Delta\theta_0}\begin{vmatrix} 0 \\ -r\Delta_2(\tau_{xx})\dfrac{\partial\theta}{\partial x}+\Delta_2(\tau_{\theta x})-r\Delta_2(\tau_{rx})\dfrac{\partial\theta}{\partial r} \\ -r\Delta_2(\tau_{x\theta})\dfrac{\partial\theta}{\partial x}+\Delta_2(\tau_{\theta\theta})-r\Delta_2(\tau_{r\theta})\dfrac{\partial\theta}{\partial r} \\ -r\Delta_2(\tau_{xr})\dfrac{\partial\theta}{\partial x}+\Delta_2(\tau_{\theta r})-r\Delta_2(\tau_{rr})\dfrac{\partial\theta}{\partial r} \\ 0 \end{vmatrix} \tag{A.9}$$

For a rotor,

$$K_{inv} \approx \frac{1}{\Delta\theta_0}\begin{vmatrix} 0 \\ r\Delta_2(p)\dfrac{\partial\theta}{\partial x} \\ -\Delta_2 p \\ r\Delta_2(p)\dfrac{\partial\theta}{\partial r} \\ -[\Delta_2(U_{wheel}p)] \end{vmatrix} \tag{A.10}$$

$$K_{vis} = \frac{1}{\Delta\theta_0}\begin{vmatrix} 0 \\ -r\Delta_2(\tau_{xx})\dfrac{\partial\theta}{\partial x}+\Delta_2(\tau_{\theta x})-r\Delta_2(\tau_{rx})\dfrac{\partial\theta}{\partial r} \\ -r\Delta_2(\tau_{x\theta})\dfrac{\partial\theta}{\partial x}+\Delta_2(\tau_{\theta\theta})-r\Delta_2(\tau_{r\theta})\dfrac{\partial\theta}{\partial r} \\ -r\Delta_2(\tau_{xr})\dfrac{\partial\theta}{\partial x}+\Delta_2(\tau_{\theta r})-r\Delta_2(\tau_{rr})\dfrac{\partial\theta}{\partial r} \\ \Delta_1(U_{wheel}\tau_{x\theta})+\Delta_2(U_{wheel}\tau_{\theta\theta})+\Delta_3(U_{wheel}\tau_{r\theta}) \end{vmatrix} \tag{A.11}$$

where in Eqs. (A.10) and (A.11), U_{wheel} is the wheel speed. From Eqs. (A.8) to (A.11), K_{inv} and K_{vis} for rotors differ from those for stators in the work input term.

Close examination of Eqs. (A.8) to (A.11) would reveal that the momentum terms are similar to the components of the pressure and viscous loading at a typical point on a blade, as illustrated by the forces $\vec{F}_{inv}$ and $\vec{F}_{vis}$ respectively in Fig. A.3.

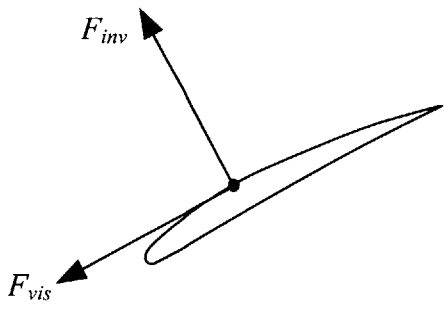

Fig. A.3 Pressure and Viscous Loading at a Typical Point

Defining $\vec{f}_{inv}$ and $\vec{f}_{vis}$ as the pressure loading and viscous force per unit mass on a blade, for stators, Eq. (A.8) can be written as

$$K_{inv} \approx \begin{vmatrix} 0 \\ r\rho f_{inv,x} \\ r\rho f_{inv,\theta} \\ r\rho f_{inv,z} \\ 0 \end{vmatrix} \tag{A.12}$$

where the components of $\vec{f}_{inv}$ are given by

$$f_{inv,x} = \Delta_2(p)\frac{1}{\rho\Delta\theta_0}\frac{\partial\theta}{\partial x} \tag{A.13}$$

$$f_{inv,\theta} = -\Delta_2(p)\frac{1}{\rho r\Delta\theta_0} \tag{A.14}$$

$$f_{inv,z} = \Delta_2(p)\frac{1}{\rho\Delta\theta_0}\frac{\partial\theta}{\partial r} \tag{A.15}$$

Also for stators, Eq. (A.9) can be written as

$$K_{vis} \approx \begin{vmatrix} 0 \\ r\rho f_{vis,x} \\ r\rho f_{vis,\theta} \\ r\rho f_{vis,z} \\ 0 \end{vmatrix} \tag{A.16}$$

where the components of $\vec{f}_{vis}$ are given by

$$f_{vis,x} = \frac{1}{\rho r \Delta\theta_0}\left[-r\Delta_2(\tau_{xx})\frac{\partial\theta}{\partial x} + \Delta_2(\tau_{\theta x}) - r\Delta_2(\tau_{rx})\frac{\partial\theta}{\partial r}\right] \tag{A.17}$$

$$f_{vis,\theta} = \frac{1}{\rho r \Delta\theta_0}\left[-r\Delta_2(\tau_{x\theta})\frac{\partial\theta}{\partial x} + \Delta_2(\tau_{\theta\theta}) - r\Delta_2(\tau_{r\theta})\frac{\partial\theta}{\partial r}\right] \tag{A.18}$$

$$f_{vis,z} = \frac{1}{\rho r \Delta\theta_0}\left[-r\Delta_2(\tau_{xr})\frac{\partial\theta}{\partial x} + \Delta_2(\tau_{\theta r}) - r\Delta_2(\tau_{rr})\frac{\partial\theta}{\partial r}\right] \tag{A.19}$$

For rotors, Eq. (A.10) can be written as

$$K_{inv} \approx \frac{1}{\Delta\theta_0}\begin{vmatrix} 0 \\ r\rho f_{inv,x} \\ r\rho f_{inv,\theta} \\ r\rho f_{inv,z} \\ r\rho f_{inv,\theta} U_{wheel} \end{vmatrix} \tag{A.20}$$

and Eq. (A.11) as

$$K_{inv} \approx \frac{1}{\Delta\theta_0}\begin{vmatrix} 0 \\ r\rho f_{vis,x} \\ r\rho f_{vis,\theta} \\ r\rho f_{vis,z} \\ r\rho f_{vis,\theta} U_{wheel} \end{vmatrix} \tag{A.21}$$

with the force components also given by Eqs. (A.13) to (A.15) and Eqs. (A.17) to (A.19).

From the preceding explanation, it can be seen that K_{inv} and K_{vis} are terms which represent blade force. The last 2 terms on the right-hand side of Eq. (A.4) represent viscous forces in the *x-r* plane. Thus the physical meaning of the body force of Eq. (A.7) is the summation of blade force and viscous force in the *x-r* plane.

APPENDIX B : CALCULATION OF BODY FORCES FROM STREAMLINE CURVATURE DATA

This appendix presents the detailed procedure for calculating body forces from streamline curvature data. Fig. B.1 shows a typical blade row for which flow properties and blockage at discrete points along the leading and trailing edges have been determined previously from streamline curvature computations [7]. Two such adjacent points 1 and 2 at the leading edge, together with corresponding points 3 and 4 on the trailing edge, are taken to form a control volume Γ with a body force $\vec{F}$.

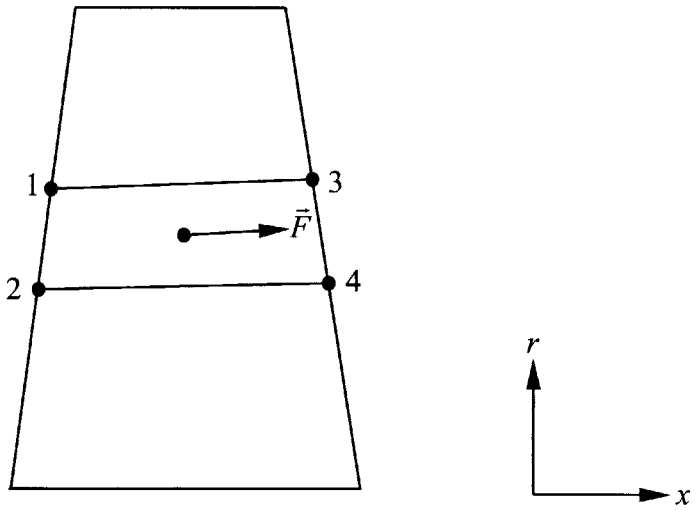

Fig. B.1 Control Volume with Body Force

$\vec{F}$ is determined using the procedure outlined in Section 2.5. This involves numerical integration of the momentum equations in Eq. (2.1) over the control

volume. Knowing that the flow field is steady, integration of Eq. (2.1) over Γ produces

$$\int_{\partial\Gamma}(b\overline{F}_{inv})dr + \int_{\partial\Gamma}(b\overline{H}_{inv})dx = \int_{\Gamma}(b\overline{S})d\Gamma + \int_{\Gamma}(r\vec{F})d\Gamma \tag{B.1}$$

where $\partial\Gamma$ is the boundary of Γ. Each component of $\vec{F}$ is determined numerically by

$$F = \frac{\sum_{edges}(b\overline{F}_{inv})\Delta r + \sum_{edges}(b\overline{H}_{inv})\Delta x - [b\overline{S}(\Delta\Gamma)]}{r_c\Delta\Gamma} \tag{B.2}$$

$\Delta\Gamma$ is the area of Γ, Δr and Δx are the radial and axial dimensions of the edges, and r_c is the r-coordinate of the centroid of Γ. Edge values of blockage b, $\overline{F}_{inv}$ and $\overline{H}_{inv}$ are taken to be simple averages of the corresponding nodal values.

The body force per unit mass $\vec{f}$ to be used in UnsComp is determined from

$$\vec{f} = \frac{1}{\overline{\rho}_{ave}}\vec{F} \tag{B.3}$$

where $\overline{\rho}_{ave}$ is the average $\overline{\rho}$ of the four nodes of Γ.

BIBLIOGRAPHY

1. Abdallah, S. and Henderson, R.E., "Improved Approach to the Streamline Curvature Method in Turbomachinery," *ASME Journal of Fluids Engineering*, Vol. 109, 1987, pp. 213-217

2. Adamczyk, J. J., "Model Equation for Simulating Flows in Multistage Turbomachinery," ASME Paper 85-GT-226, 1985

3. Adamczyk, J. J., "Aerodynamic Analysis of Multistage Turbomachinery Flows in Support of Aerodynamic Design," *ASME Journal of Turbomachinery*, Vol. 122, 2000, pp. 189-217

4. Bell, D. L., and He L., "Three-Dimensional Unsteady Flow for an Oscillating Turbine Blade and the Influence of Tip Leakage," *ASME Journal of Turbomachinery*, Vol. 122, 2000, pp. 93-101

5. Choi, T. J., "Development of an Effective Computational Methodology for Multistage Compressor Map Generation," S.M. Thesis, Massachusetts Institute of Technology, July 2001

6. Dawes, W. N., "Towards Improved Throughflow Capability: The Use of 3D Viscous Flow Solvers in a Multistage Environment," *ASME Journal of Turbomachinery*, Vol 114, 1992, pp 8-17

7. Denton, J. D., "Throughflow Calculations for Transonic Axial Flow Turbines," *ASME Journal of Engineering for Gas Turbines and Power*, Vol. 100, 1978, pp. 212-218

8. Denton, J.D., and Dawes, W.N., "Computational Fluid Dynamics for Turbomachinery Design," *IMechE Journal of Mechanical Engineering Science*, Vol. 213, No. C2, 1999, pp. 107-124

9. Dorney, D. J., Griffin, L. W. and Huber, F. W., "A Study of the Effects of Tip Clearance on a Supersonic Turbine," *ASME Journal of Turbomachinery*, Vol. 122, 2000, pp. 674-683

10. Dring, R. P. and Spear, D. A., "The Effects of Wake Mixing on Compressor Aerodynamics," *ASME Journal of Turbomachinery*, Vol. 113, 1991, pp. 600-607

11. Escuret, J. F., and Garnier, V., "Numerical Simulations of Surge and Rotating Stall in Multistage Axial-flow Compressors," AIAA Paper 94-3202, June 1994

12. Gerolymos, G. A., and Hanisch, C., "Multistage 3-D Navier-Stokes Computation of Off-Design Operation of a 4-Stage Turbine," *IMechE Journal of Power and Energy*, Vol. 213, 1999, pp. 243-261

13. Gong, Y., "A Computational Model for Rotating Stall and Inlet Distortions in Multistage Compressors," Ph.D. Thesis, Massachusetts Institute of Technology, March 1999

14. Greitzer, E. M., "Surge and Rotating Stall in Axial Flow Compressors; Part 1: Theoretical Compression System Model," *ASME Journal of Engineering for Gas Turbines and Power*, Vol. 98, No. 2, 1976, pp. 190-198

15. Greitzer, E. M., "Surge and Rotating Stall in Axial Flow Compressors; Part 2: Experimental Results and Comparison with Theory," *ASME Journal of Engineering for Gas Turbines and Power*, Vol. 98, No. 2, 1976, pp. 199-217

16. Greitzer, E. M., "Inlet Distortion Effects in Axial Compressors," VKI Lecture Series on Unsteady Flow in Turbomachines, Jan. 1979

17. Hirsch, C. and Denton, J. D., "Throughflow Calculations in Axial Turbomachinery," AGARD AR 175, 1981

18. Horlock, J. H., and Marsh, H., "Flow Models for Turbomachines," *IMechE Journal of Mechanical Engineering Science*, Vol. 13, No.5, 1971, pp.358-368

19. Hynes, T. P., and Greitzer, E. M., "A Method for Assessing Effects of Inlet Flow Distortion on Compressor Stability," *ASME Journal of Turbomachinery*, Vol. 109, 1987, pp. 371-379

20. Jameson, A., Schmidt, W., and Turkel, E., "Numerical Solution of the Euler Equations by Finite Volume Methods Using Runge-Kutta Time Stepping Schemes," AIAA Paper 81-1259, 1981

21. Lieblein, S., "Experimental Flow in Two-Dimensional Cascades," *Aerodynamic Design of Axial-Flow Compressors*, NASA SP-36, 1965, pp. 183-226

22. Longley, J. P., and Greitzer, E. M., "Inlet Distortion Effects in Aircraft Propulsion System Integration," Paper #6, AGARD Lecture Series #183, *Steady and Transient Performance Prediction of Gas Turbine Engines*, May 1992

23. Marble, F. E., "Three-Dimensional Flow in Turbomachines," *Aerodynamics of Turbines and Compressors, Vol X of High Speed Aerodynamics and Jet Propulsion*, Hawthorne, W. R., ed. Princeton University Press, Princeton, N. J., 1964, pp. 83-166

24. Marsh, H., "A Digital Computer Program for the Through-Flow Fluid Mechanics in an Arbitrary Turbomachine Using a Matrix Method," *Aeronautical Research Council*, R and M 3509, 1968

25. Smith, L. H., "The Radial-Equilibrium Equations for Turbomachinery," *ASME Journal of Engineering for Gas Turbines and Power*, Vol. 88, 1966, pp. 1-12

26. Volmar, T. W., Brouillet, B., Gallus, H. E. and Benetschik, H., "Time-Accurate 3-D Navier-Stokes Analysis of 1 1/2-Stage Axial-Flow," *AIAA Journal of Propulsion and Power*, Vol. 16, 2000, pp. 327–335